AIP Publishing Physics of Fluids ACCEPTED MANUSCRIPT
This is the author's peer reviewed, accepted manuscript. However, the online version of record will be different from this version once it has been copyedited and typeset.
PLEASE CITE THIS ARTICLE AS DOI: 10.1063/5.0332888

Modeling the compressible flow field of an impulsively started circular cylinder with refined potential flow theory

Taofiq Omoniyi Amoloye,[1] Leke Thaddeus Oladimeji,[1] Mahmoud A. Hayajnh,[2] and Olalekan Adebayo Olayemi[1]
[1)]*Department of Aeronautical and Astronautical Engineering, Faculty of Engineering and Technology, Kwara State University, Malete, Nigeria.*
[2)]*Department of Aeronautical Engineering, Jordan University of Science and Technology, Irbid, Jordan 22110.*

(*Electronic mail: taofiq.amoloye@kwasu.edu.ng)

(*Electronic mail: leke.oladimeji14@gmail.com)

(*Electronic mail: mahayajnh@just.edu.jo)

(*Electronic mail: olalekan.olayemi@kwasu.edu.ng)

(Dated: 3 July 2026)

Understanding compressible flows over bluff bodies, such as circular cylinders, is critical for applications in aerospace engineering, space exploration, and astrophysics. However, the complexity of viscous and unsteady flows, compounded by compressibility effects, remains a challenge for experimental and computational methods. This study explores the compressible flow field of an impulsively started circular cylinder using Refined Potential Flow Theory (RPT), an analytical model that extends classical potential flow theory to include compressibility effects. The governing equations, boundary conditions, and refined stream function are developed to capture the density, velocity, and pressure fields in subsonic and transonic regimes. The results demonstrate that compressibility marginally increases vortex enstrophy at low Reynolds numbers, while its influence on wake flow stability diminishes at higher values. The study reveals that compressibility suppresses shear layer instability, reduces wake velocity deficits, and introduces smaller-scale structures that disrupt the inertial range of turbulence in the low subsonic regime. At higher Mach numbers ($M_\infty \geq 0.6$), local supersonic pockets and shock waves emerge, forming complex λ-shock systems and bow shocks. The predictions of the Strouhal number from RPT show marginal changes for $0.2 \leq M_\infty \leq 0.5$, consistent with experimental and computational trends. Although RPT aligns with existing methods to capture key flow features, discrepancies in wake stability and recirculation zone dimensions highlight areas for further refinement. This research underscores the potential of RPT in developing optimization tools to complement experimental and numerical studies, offering valuable insights into compressible flow physics for engineering applications in high-altitude flight and space exploration.

PACS numbers: 35Q30, 76D03, 76D05, 76N10, 76-10, 31-02, 35D99, 00A06, 76F05

I. INTRODUCTION

Knowledge of compressible flows over bluff bodies, such as circular cylinders and spheres, is important for many applications, including high-altitude unmanned aircraft design[1], astrophysics[2,3], and interplanetary space exploration[1,4]. However, the complexity of viscous and unsteady cylinder flows[5–7] is usually compounded by compressibility effects[8]. This is not well understood[9]. Early studies of cylinder flows focused on the incompressible regime. This is because the operational envelope of the wind tunnel is usually limited to the low Reynold number (*Re*: based on the freestream velocity, V_∞, the cylinder diameter, D, and the fluid kinematic viscosity, ν, as $Re = V_\infty D/\nu$) and the low compressible subsonic flow range[4]. These studies, including those by Taneda[10], Dennis and Chang[11], Coutanceau and Bouard[12,13], Roshko[14,15], Parnadeau et al.[16], and Behara and Mittal[17], characterize the wake phenomenon with *Re* with other unique properties for each condition. These confirm that the flow around a circular cylinder is strongly dependent on *Re*.

Experiments show that the force coefficients in sub-critical cylinder flow depend on both *Re* and M_∞ (freestream Mach number, $M_\infty = V_\infty/a_\infty$ where a_∞ is the speed of sound in the freestream) in the subsonic compressible regime[18,19]. However, the influence of *Re* fades as the flow becomes supersonic for both the sub-critical and super-critical regimes[19]. Wake transitions in the supersonic sub-critical regime have been experimentally studied[20]. Although the Strouhal number was experimentally examined as 0.18 for $M_\infty < 0.9$, the wake periodicity or discernible vortex shedding breaks down for $M_\infty > 0.9$ in the range *Re* between $30,000$ and $500,000$[21]. A strong coupling effect has been observed between M_∞ and the vortex street in the near wake for subsonic compressible and transonic cylinder flows in the *Re* range from 0.8 to $2,000,000$[22]. The strength of the wake vortices changes at $M_\infty > 0.6$, reducing the base pressure drag until $M_\infty > 0.9$ where local sonic flows present increased drag[23]. Experimental studies of subsonic compressible flow in the intermediate sub-critical regime *Re* have characterized the compressibility effects on the location of the shedding of the von Kármán vortices, the frequency of shedding, and the maximum width of the recirculation region for circular cylinders[1,24] and spheres[25].

Computational fluid dynamics (CFD) studies have contributed to the exploration of compressible flow over a circular cylinder[26–31]. Canuto and Taira[32] observed that compressibility effects lower the dominant frequency and growth rate of flow instability in the linear growth stage for $M_\infty \leq 0.5$ in

AIP Publishing Physics of Fluids ACCEPTED MANUSCRIPT
This is the author's peer reviewed, accepted manuscript. However, the online version of record will be different from this version once it has been copyedited and typeset.
PLEASE CITE THIS ARTICLE AS DOI: 10.1063/5.0332888

the low *Re* regime. In this regime, Liu et al.[33] also observed that compressibility effects enhance flow stability, presenting a reduction in vortex shedding strength, shedding frequency, and aerodynamic force fluctuations as M_∞ increases. Shang[34] observed rapid and extreme variations in the flow field at $M_\infty = 0.6$ and $Re = 167,000$, with large-scale structures contributing significantly to turbulence in the wake. Qualitative agreement was observed for the general flow features. The results of Ishii and Kuwahara show that compressibility suppresses the width of the wake[35]. Pandolfi and Larocca[36] show that half cylinders experience separation behind shocks in transonic flows, whereas full cylinders show asymmetric, unsteady, periodic flows. Botta's solution[37] has periodic behavior at M_∞ between 0.5 and 0.6, undergoing two transitions as M_∞ increases from 0.6 to 0.98. Shirani[38] observed that for $M_\infty > 0.6$, the flow parameters become independent of *Re*, while at $M_\infty > 0.8$, they become independent of M_∞. Xu et al.[39] demonstrated that above a critical $M_\infty \approx 0.9$, the flow is a quasi-steady flow with virtually stationary shock waves created in the near wake. Below this critical M_∞, there exists an unsteady flow with moving shock waves interacting with the turbulent flow in the cylinder near wake. These drastic changes in the flow field near high-subsonic and transonic regimes have also been reported by others[40]. At $Re = 10,000$, compressibility significantly affects the location and mechanism of the transition. The wake transition region shifts towards the cylinder shoulder as M_∞ increases, with an eventual loss of wake coherence and the vortex shedding frequency[41]. Compressibility also affects the dimensionality of the flow at low *Re*, stabilizing the instability of mode B and delaying the three-dimensionalization of the wake as M_∞ increases[42]. At $Re = 3,900$, compressibility suppresses the Kelvin-Helmholtz instability but increases velocity fluctuations in the boundary layer and the pressure difference between the freestream and the recirculation zone[43]. Consequently, the recirculation zone shortens with M_∞ up to 0.5.

From the foregoing review it can be seen that numerous amounts of work have been done to evaluate the effect of compressibility on a circular cylinder experimentally and numerically, both of which have documented limitations[1,44]. Hence, there is a need to consider other approaches. The Janzen-Rayleigh expansions[45] of the flow variables as functions of M_∞ are the earliest attempts to theorize compressible flow over a circular cylinder. These were applied to study the d'Alembert's paradox in the subsonic compressible flow regime, assuming a steady, inviscid flow of a polytropic fluid with no external forces or initial vorticity[45]. Consequently, this formulation cannot replicate the foregoing features of the full range of the unsteady, viscous, and compressible flow of an impulsively started circular cylinder. These features are physical solutions of the governing equations that are coupled and notoriously non-linear, resisting general analytical descriptions of the entire flow[46]. Cherry and Temple[47] attempted an exact solution of a two-dimensional subsonic compressible flow around a cylinder. However, there were non-physical discontinuities within the flow, and the full physics of the phenomena was not captured or reported. Joseph[48,49] explored viscous potential flows (VPF) as solutions to the governing equations, focusing on the inclusion of viscous normal stresses in the definition of pressure[49] and extending the VPF into the compressible flow regime for sound waves in a perturbation analysis of the linearized governing equations in a state of rest[48]. However, the applications of VPF analysis[50] do not include compressible flow over a circular cylinder. Amoloye[5] successfully refined the classical potential flow theory for cylinder flows to model the wake characteristics of an impulsively started circular cylinder in the sub-critical regime. The model focuses on the incompressible flow. However, there are unpublished extensions of the formulation to include compressibility effects[51–54].

Therefore, the present publication seeks to explore the refined potential flow theory (RPT) in the study of compressible flow over an impulsively started circular cylinder in the subcritical regime, attempting to theorize subsonic compressible and transonic flow physics. This analytical model can aid the development of optimization tools to complement numerical and experimental studies for engineering applications in space exploration and high-altitude unmanned aerial vehicle missions. It can also offer insights into compressible flow over blunt objects with potential applications in space physics and astrophysics[3,46].

Section II discusses the governing equations and boundary conditions. Section III develops RPT for compressible circular cylinder flows. Instantaneous streamline patterns of RPT, time-averaged flow field velocity profiles, wake velocity energy spectra, and predicted Strouhal numbers are reported and discussed in comparison with published results from experiments and CFD in Section IV. Section V concludes the paper.

II. GOVERNING EQUATIONS AND BOUNDARY CONDITIONS

Assuming an isotropic and Newtonian fluid in an infinite domain, the governing equations for the compressible cylinder crossflow considered here are the continuity equation

$$\frac{\partial \rho}{\partial t} + \nabla \cdot (\rho \mathbf{V}) = 0 \quad (t \geq 0), \tag{1}$$

the compressible Navier-Stokes equations (NSE)

$$\frac{\partial (\rho \mathbf{V})}{\partial t} + \mathbf{V}\nabla \cdot (\rho \mathbf{V}) + (\rho \mathbf{V}) \cdot \nabla \mathbf{V} = -\nabla p + \nabla ([\lambda + 2\mu] \nabla \cdot \mathbf{V}) + \nabla \times (\mu \omega) \quad (t \geq 0), \tag{2}$$

and the energy equations

$$\frac{\partial (\rho E)}{\partial t} + \nabla \cdot (\rho \mathbf{V} E + P\mathbf{V}) = \nabla \cdot (k \nabla T) + \nabla \cdot (\mathbf{V} [\nabla ([\lambda + 2\mu] \nabla \cdot \mathbf{V}) + \nabla \times (\mu \omega)]) \quad (t \geq 0) \tag{3}$$

ACCEPTED MANUSCRIPT
Physics of Fluids
AIP Publishing
This is the author's peer reviewed, accepted manuscript. However, the online version of record will be different from this version once it has been copyedited and typeset.
PLEASE CITE THIS ARTICLE AS DOI: 10.1063/5.0332888

where $\mathbf{V}$ is the velocity, p is the pressure, ρ is the density, ω is the vorticity vector, λ is the second coefficient of viscosity, μ is the dynamic viscosity, E is the total energy, k is the thermal conductivity, T is the temperature, and t is the dimensional time[55,56]. Together, Eqs. 1 to 3 constitute an initial boundary value problem. The boundary conditions on the velocity are the infinity boundary condition at the freestream and the no-slip boundary condition at the cylinder surface.

III. REFINED POTENTIAL FLOW THEORY FOR COMPRESSIBLE FLOWS OVER CIRCULAR CYLINDERS

For an incompressible circular cylinder flow, Eqs. 1 and 2 reduce to

$$\nabla \cdot \mathbf{V} = 0 \quad (t \geq 0), \tag{4}$$

and

$$\begin{aligned} &\frac{\partial \mathbf{V}}{\partial t} + \nabla\left(\frac{p}{\rho} + \frac{V^2}{2} - \left[\frac{\lambda}{\rho} + 2\nu\right]\nabla \cdot \mathbf{V}\right) \\ &= \mathbf{V} \times \omega + \nabla \times (\nu\omega) \quad (t \geq 0) \end{aligned} \tag{5}$$

respectively, where $V = |\mathbf{V}|$ and $\nu = \mu/\rho$. These constitute the Navier-Stokes problem[57,58].

A rotational velocity field satisfying Eq. 4 is obtained from a vector of unsteady, planar, and viscous stream function, $\vec{\psi}$, as

$$\mathbf{V} = \nabla \times \vec{\psi}, \tag{6}$$

where $\vec{\psi} = \psi_{vis}\hat{\mathbf{e}}_z$[5] (vis: viscous). However , Eq. 6 describes a planar flow whereas an actual cylinder flow is three-dimensional. For three-dimensional consideration in RPT, the distinction between Cartesian geometric coordinate axes of the flow domain and Cartesian wind coordinate axes (signified by the tilde) is introduced[5]. The three-dimensional Cartesian geometric coordinate axes are

$$x = r\cos\theta\sin\varphi \quad y = r\sin\theta\sin\varphi \quad z = r\cos\varphi \tag{7}$$

where r, θ, and φ are the radial, circumferential, and azimuthal coordinate variables of an associated spherical geometric coordinate system, respectively. However, the Cartesian wind coordinate axes are

$$\begin{aligned} &\tilde{x} = r\cos\theta\sin\tilde{\varphi} \quad \tilde{y} = r\sin\theta\sin\tilde{\varphi} \quad \tilde{z} = r\cos\tilde{\varphi} = 0 \\ &\tilde{\varphi} = \frac{\pi}{2} \quad V_{\tilde{z}} = 0 \quad V_{\tilde{\varphi}} = 0\ . \end{aligned} \tag{8}$$

This system of axes is perpetually two-dimensional, that is, $\tilde{z}$ is always zero. For every φ plane, there is a coincident $\tilde{\varphi}$ plane of the wind axes that has a constant value $\pi/2$ as depicted in Fig. 1. $V_{\tilde{z}} = V_{\tilde{\varphi}} = 0$ for all these planes. The geometric axes of ψ_{vis} are therefore transformed into the wind axes for a rotational symmetry of the flow in the three-dimensional space[5].

In terms of $\vec{\psi}$, Eq. 5 becomes

$$\begin{aligned} &\nabla \times \frac{\partial \vec{\psi}}{\partial t} + \nabla\left(\frac{p}{\rho} + \frac{|\nabla \times \vec{\psi}|^2}{2} - \left[\frac{\lambda}{\rho} + 2\nu\right]\nabla \cdot (\nabla \times \vec{\psi})\right) \\ &= (\nabla \times \vec{\psi}) \times \omega + \nabla \times (\nu\omega) \end{aligned} \tag{9}$$

clearly presenting the difficulty of analytically obtaining a corresponding pressure field that conserves momentum.

A three-dimensional viscous potential function for which $\omega = 0$ overcomes the difficulty presented in Eq. 9[5,49]. Thus, to render the velocity field from ψ_{vis} quasi-irrotational in the Cartesian wind coordinate system, ψ_{vis} is defined on a principal axis of the flow about which ω is identically zero[5]. The preceding transformations define $\tilde{\kappa}$, an incompressible quasi-potential stream function for the cylinder flow in RPT[5]. $\tilde{\kappa}$ has the properties of a stream function in a cylindrical polar coordinate system that allow it to satisfy the conservation of mass (Eq. 4) and produce a rotational velocity field . Also, it has the properties of a potential function in the Cartesian wind coordinate axes (see appendix A for more details) that satisfy the incompressible NSE and help to conserve momentum as

$$\begin{aligned} &\mathbf{V} = \nabla\tilde{\kappa} \\ &\nabla\left(\frac{\partial\tilde{\kappa}}{\partial t} + \frac{p}{\rho} + \frac{|\nabla\tilde{\kappa}|^2}{2} - \left[\frac{\lambda}{\rho} + 2\nu\right]\nabla^2\tilde{\kappa}\right) = 0 \quad (t \geq 0) \end{aligned} \tag{10}$$

because the pressure field is scalar and invariant to coordinate transformations.

$\tilde{\kappa}$ is a solution of Laplace's equation, satisfying the viscous boundary conditions and incorporating unsteady characteristics of the cylinder wake flow[5]. Some of these characteristics including the Strouhal number and the energy cascade correlate agreeably with CFD and experiments in the Reynolds number and non-dimensional time ranges of $30 < Re < 10{,}000$ and $0.2 \leq V_\infty t/R \leq 77{,}047$ respectively[5] (where R is the radius of the cylinder).

Amoloye[5] provides details of the refinement of the classical potential flow theory of a cylinder flow and the derivation of $\tilde{\kappa}$. Here, a compressible form of $\tilde{\kappa}$ is defined as

$$\kappa = \rho\tilde{\kappa} \tag{11}$$

to include compressibility effects. Attention is focused on the process of propagating sound waves to describe the density field. This process is a one-dimensional steady isentropic one that is governed by the combined continuity and Euler's equation

$$\frac{d\rho}{\rho} = -\frac{d(V^2)}{2a^2} \tag{12}$$

where a is the local speed of sound. Substituting the corresponding energy equation for a polytropic gas

$$a^2 = a_0^2 - \frac{\gamma - 1}{2}V^2 \ , \tag{13}$$

gives a first order partial differential equation in terms of ρ and V^2 as

$$\frac{d\rho}{\rho} = -\frac{1}{2\left(a_0^2 - \frac{\gamma-1}{2}V^2\right)}d(V^2) \tag{14}$$

where a_0 is the stagnation speed of sound, γ is the ratio of specific heats, and V is obtained from the incompressible flow

ACCEPTED MANUSCRIPT
Physics of Fluids
AIP Publishing
This is the author's peer reviewed, accepted manuscript. However, the online version of record will be different from this version once it has been copyedited and typeset.
PLEASE CITE THIS ARTICLE AS DOI: 10.1063/5.0332888

i.e. $\tilde{\kappa}$. Although, sound propagation is analytically modeled as a one-dimensional process, Eq. 12 applies independently in each dimension because sound propagates radially outwards from a source and Euler's equation applies throughout the flow field, not just on a streamline[55]. Equations 12 and 14 are also employed to obtain the full velocity potential equation in standard textbooks on aerodynamics[55,59]. The difference in the approach here is that V is a known quantity from $\tilde{\kappa}$, which makes Eq. 14 analytically integrable. Just before the impulsive start, a_0 equals a_∞. Therefore, the density field

$$\frac{\rho}{\rho_\infty} = \left(\frac{1 - \frac{\gamma-1}{2} M_\infty^2}{1 - \frac{\gamma-1}{2} M^2} \right)^{\frac{1}{\gamma-1}} \tag{15}$$

is analytically integrated from the differential equation. The local Mach number, M, is equal to V/a_∞.

The velocity components in the cylindrical coordinate system are derived as

$$\left\{ \begin{array}{c} V_r \\ V_\theta \\ V_z \end{array} \right\} = \frac{1}{\rho} \nabla \times \overrightarrow{\kappa} = \left\{ \begin{array}{c} \frac{1}{\rho r} \frac{\partial \kappa}{\partial \theta} \\ -\frac{1}{\rho} \frac{\partial \kappa}{\partial r} \\ 0 \end{array} \right\}, \tag{16}$$

and in the Cartesian wind coordinate system as

$$\left\{ \begin{array}{c} V_{\tilde{x}} \\ V_{\tilde{y}} \\ V_z \end{array} \right\} = \frac{1}{\rho} \nabla \kappa = \left\{ \begin{array}{c} \frac{1}{\rho} \frac{\partial \kappa}{\partial x} \\ \frac{1}{\rho} \frac{\partial \kappa}{\partial y} \\ \frac{1}{\rho} \frac{\partial \kappa}{\partial z} \end{array} \right\}. \tag{17}$$

Eqs. 16 and 17 are not equivalent, but the magnitude of the physical velocity field that they describe is invariant to coordinate transformation.

κ satisfies the conservation of mass in

$$\begin{aligned} & \oint_{\mathscr{V}} \left[\frac{\partial \rho}{\partial t} + \underbrace{\nabla \cdot (\rho \mathbf{V})}_{=0} \right] d\mathscr{V} \\ &= \frac{\partial}{\partial t} \left[\oint_{\mathscr{V}} \rho \, d\mathscr{V} \right] \\ &= 0 \quad (t \geq 0), \end{aligned} \tag{18}$$

because the volume integral of the transient variation of the density is zero in the infinite domain.

Using a vector identity[60], the third term on the left-hand side of Eq. 2 is expanded and simplified as

$$\begin{aligned} & [(\rho \mathbf{V}) \cdot \nabla \mathbf{V}] \\ &= \nabla (\rho \mathbf{V} \cdot \mathbf{V}) - \mathbf{V} \cdot \nabla (\rho \mathbf{V}) \\ & - \mathbf{V} \times (\nabla \times \rho \mathbf{V}) - \rho \mathbf{V} \times (\nabla \times \mathbf{V}) \\ &= \nabla (\rho \mathbf{V} \cdot \mathbf{V}) - \mathbf{V} \cdot \nabla (\rho \mathbf{V}) \\ & - \mathbf{V} \times (\nabla \times \nabla \kappa) - \rho \mathbf{V} \times \boldsymbol{\omega}. \end{aligned} \tag{19}$$

In the Cartesian wind coordinate axes, $\mathbf{V} \times (\nabla \times \nabla \kappa)$ is equal to zero because the curl of the gradient of a scalar field is a zero vector. $\rho \mathbf{V} \times \boldsymbol{\omega}$ is also equal to zero because κ is a quasi-potential function in these axes. Thus, Eq. 2 reduces to

$$\frac{\partial (\rho \mathbf{V})}{\partial t} + \nabla (\rho \mathbf{V} \cdot \mathbf{V}) = -\nabla p + \nabla ([\lambda + 2\mu] \nabla \cdot \mathbf{V}) \quad (t \geq 0). \tag{20}$$

Using Eq. 17, the conservation of momentum yields the pressure field as

$$p = -\frac{\partial \kappa}{\partial t} - \rho \left| \frac{\nabla \kappa}{\rho} \right|^2 + [\lambda + 2\mu] \nabla \cdot \left(\frac{\nabla \kappa}{\rho} \right) + F(t) \tag{21}$$

where $F(t)$ is a function of time that is taken to be the total pressure of the free stream, p_0.

When $\mathbf{V} = 0$ (the surface no-slip condition), the pressure field must satisfy the hydrostatic pressure condition in which the sum of the normal stresses on the principal axes is a tensor invariant[48,49,56]. The mechanical pressure[56] (or the mean pressure[61]), $\tilde{p}$, is defined as a negative one-third of the sum of the normal stresses on a fluid element. Thus, rearranging Eq. 21 by separation of the isotropic and deviatoric parts of the stress component and taking the mean gives

$$p = -\frac{\partial \kappa}{\partial t} - \rho \left| \frac{\nabla \kappa}{\rho} \right|^2 + \frac{4}{3} \mu \nabla \cdot \left(\frac{\nabla \kappa}{\rho} \right) + \left(\lambda + \frac{2}{3} \mu \right) \nabla \cdot \left(\frac{\nabla \kappa}{\rho} \right) + p_0 \tag{22}$$

so that

$$\tilde{p} = \left[\frac{\partial \kappa}{\partial t} + \rho \left| \frac{\nabla \kappa}{\rho} \right|^2 - \frac{4}{3} \mu \nabla \cdot \left(\frac{\nabla \kappa}{\rho} \right) - p_0 \right] - \left(\lambda + \frac{2}{3} \mu \right) \nabla \cdot \left(\frac{\nabla \kappa}{\rho} \right). \tag{23}$$

The expression in the square brackets is negative of the thermodynamic pressure field. Equation 23 is dimensionally con-

ACCEPTED MANUSCRIPT
Physics of Fluids
AIP Publishing
This is the author's peer reviewed, accepted manuscript. However, the online version of record will be different from this version once it has been copyedited and typeset.
PLEASE CITE THIS ARTICLE AS DOI: 10.1063/5.0332888

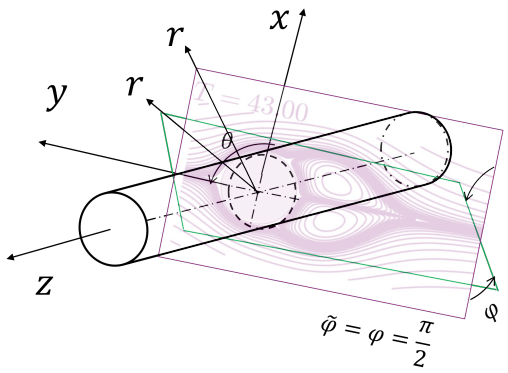


FIG. 1: The geometric and wind coordinate axes in relation to ψ_{vis}[5]. Reproduced with permission from Phys. Scr. **99** 085207 (2024). Copyright 2024 IOP Publishing Ltd.

TABLE I: Cylinder radius and flow conditions.

Radius, R (m)	ν_∞ $(m^2 s^{-1})$	μ_g $(m^3 s^{-2})$
0.047	1.46069×10^{-5}	6.82×10^{-11}

sistent (see Appendix B for details) .

Stokes' hypothesis[56] assumes that λ is

$$\lambda = -\frac{2}{3}\mu \ . \tag{24}$$

However, κ is defined on the principal axes of the flow where the vorticity vector is identically zero[5]. Thus, λ and the viscous normal stresses are significant[48,49,56,61,62] in Eq. 23. Quantitative analyses on λ and the pressure field in RPT are the subject of further publications.

IV. RESULTS AND DISCUSSION

The conditions presented in table I were used for the evaluation of the results unless otherwise stated. The choices for R and the wake analogy factor, μ_g, are informed by a preceding study of the incompressible cylinder flow with RPT[5]. ν_∞ is for air at a temperature of about 15°c. In another work[63], the sensitivity of RPT to ν is explored, showing that the appropriate selection of ν is critical to influence flow stability, symmetry and energy spectra. This is similar to tuning artificial viscosity in some CFD simulations[63]. The γ values used for the test cases are typical values in aerospace ($\gamma = 1.4$; $\gamma = 1.67$)[64,65] and astrophysical ($\gamma = 1.67$; $\gamma = 3.00$)[3,46,66–68] applications. However, the specific combinations of the values of these two variables serve as parametric studies and may not correspond to an achievable physical scenario. All results are for the $z/D = 0$ plane, corresponding to a two-dimensional flow.

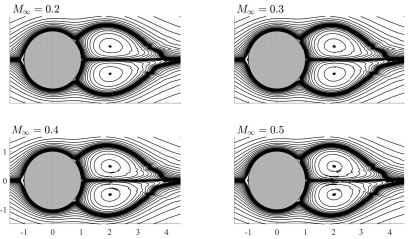


FIG. 2: Instantaneous streamlines for varying M_∞ at $Re = 34$ and $t = 43R/V_\infty$.

The subtle effect of compressibility at low Re is presented in figure 2 that shows the instantaneous streamline contours (in the cylinder reference frame) of compressible flow in RPT at $Re = 34$, $t = 43R/V_\infty$, and at varying M_∞. As M_∞ progresses, the strength of the wake bubbles increases evidently from the tightening of the streamlines around the eyes of the vortices. Consequently, the flow around the wake centerline becomes progressively distorted. This agrees with the observation in the literature that compressibility marginally increases vortex enstrophy[69].

Similar observations can be made from figure 3 showing the RPT streamline contours of compressible flow at $Re = 3,900$, $t = 3R/V_\infty$, $\gamma = 1.4$ and varying M_∞. A significantly lower viscosity value compared to Amoloye's analysis[5] was used to delay the vortex shedding and allow a comparison with the CFD results of Xue et al.[43]. Whereas Xue et al.[43] (figure 17, p. 12) present a regression in the length of the recirculation zone with a progression in M_∞ in the range $0.2 \leq M_\infty \leq 0.5$, the RPT results show a nearly constant streamwise dimension of the recirculation zone, in agreement with Nagata et al.'s[1] experimental results at $Re = 2,000$. This suggests an insensi-

AIP Publishing Physics of Fluids ACCEPTED MANUSCRIPT
This is the author's peer reviewed, accepted manuscript. However, the online version of record will be different from this version once it has been copyedited and typeset.
PLEASE CITE THIS ARTICLE AS DOI: 10.1063/5.0332888

tivity of the RPT wake flow stability to M_∞ at $Re = 3,900$ contrary to the CFD results[43]. This insensitivity is due to the use of a constant viscosity in the model. Compressibility increases the local temperature and consequently μ, as M_∞ progresses. The more viscous the fluid, the shorter the recirculation zone. This process is treated in the CFD results with a coupling of the energy equation and Sutherland's law in the simulation[43], whereas the present RPT results do not feature this. Nevertheless, RPT captures the existence and growth in intensity with M_∞ of a secondary recirculation flow structure at the back of the cylinder similar to CFD[43].

The streamwise extent of the primary recirculation region captured at $Re = 3,900$, which is nearly constant throughout the sampled M_∞, is generally approximately smaller by a diameter magnitude for the RPT compared to the CFD results of Xue et al.[43]. There is a match at $M_\infty = 0.5$, where the length of the recirculation zone is the shortest for the CFD results. The length of the recirculation region has a bearing on the shape of the time-averaged streamwise velocity profiles at different stations within the wake, as presented in figure 4 for varying M_∞ at $Re = 3,900$, $\nu = 1.46069 \times 10^{-8} m^2/s$, and $\gamma = 1.4$. Figure 5 also shows the time-averaged crossflow velocity in a cylinder wake under the same conditions. In these figures, Kravchenko and Moin's[70] experimental results of the incompressible flow at the same *Re* have been included for a complete comparison. From the first downstream station on the figures, every successive profile has been shifted by -1 from the preceding one. The RPT averages were numerically obtained from instantaneous samples in the non-dimensional time range $1 \leq V_\infty t/R \leq 77,047$ using the default settings of an in-built integrator in *Matlab*™[71]. $\tilde{x}$ and $\tilde{y}$ in these figures are equivalent to x and y respectively in the experimental data[5,70]. Outlier points[5] at the base of the trough were left out to aid in a general assessment of the shape of the profiles. The streamwise velocity profiles after $\tilde{x}/D = 0.58$ are generally V-like for the sampled M_∞, characterizing the short recirculation zones in figure 3. In particular, the shape of the $\tilde{x}/D = 1.06$ profile is consistent up to $M_\infty = 0.5$, while its outline is sensitive to variations in M_∞ in the CFD results[43]. Since the length of the recirculation bubble and the consequent shape of the velocity profile are determined by the shear layer transition[43], the consistency of the V-shaped streamwise velocity profile in the near wake seems suggestive of a marginal effect of compressibility on the shear layer transition in RPT at $Re = 3,900$ for $M_\infty \leq 0.5$. Additionally, figure 5 shows insignificant changes in the crossflow velocity profile for $0.2 \leq M_\infty \leq 0.5$. However, at $\tilde{x}/D = 2.02$, it is evident that compressibility reduces the velocity deficit in the RPT wake. This agrees with CFD result at similar conditions at the same downstream location[43] (figure 16, p. 11).

Further in the wake, compressibility increases vortex enstrophy in agreement with CFD observations[69], exacerbating the outlier points[5]. This is revealed when going from left to right in figure 6 that shows time-averaged streamwise velocity in a cylinder wake for varying M_∞ at $Re = 3,900$, $\nu = 1.46069 \times 10^{-8} m^2/s$, and $\gamma = 1.4$. The profiles are presented for several downstream locations in the wake. From $\tilde{x}/D = 0.58$, each successive profile is shifted upwards by

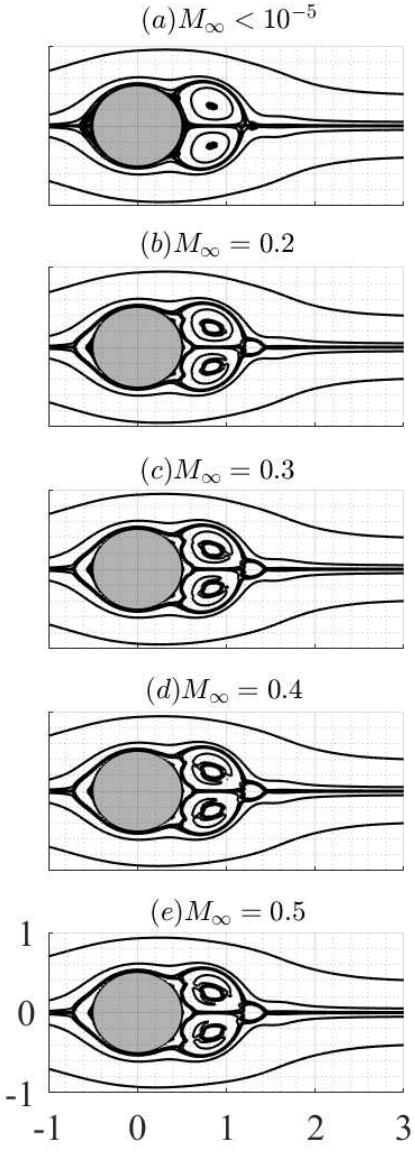


FIG. 3: Instantaneous streamlines for varying M_∞ at $Re = 3,900$ and $t = 3R/V_\infty$.

ACCEPTED MANUSCRIPT
Physics of Fluids
AIP Publishing
This is the author's peer reviewed, accepted manuscript. However, the online version of record will be different from this version once it has been copyedited and typeset.
PLEASE CITE THIS ARTICLE AS DOI: 10.1063/5.0332888

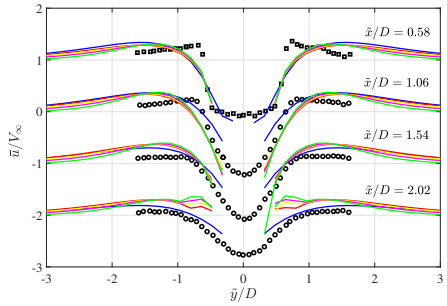


FIG. 4: Time-averaged streamwise velocity in a cylinder wake for varying M_∞ at $Re = 3,900$. $M_\infty < 10^{-5}$ (−); $M_\infty = 0.2$ (−); $M_\infty = 0.3$ (−); $M_\infty = 0.4$ (−); $M_\infty = 0.5$ (−)

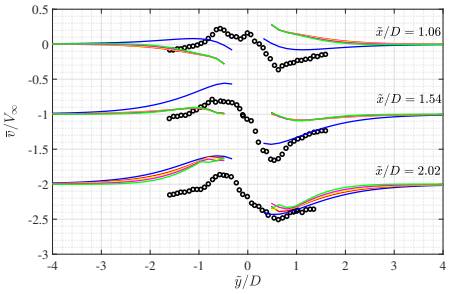


FIG. 5: Time-averaged crossflow velocity in a cylinder wake for varying M_∞ at $Re = 3,900$. $M_\infty < 10^{-5}$ (−); $M_\infty = 0.2$ (−); $M_\infty = 0.3$ (−); $M_\infty = 0.4$ (−); $M_\infty = 0.5$ (−)

−1 for clarity. The averaging period is the same as in figure 4. Figures 7 and 8 present similar plots at the same conditions for $Re = 56$ and $Re = 9,500$, respectively. An irregular pattern of velocity deficit and acceleration is experienced for $\tilde{x}/D \geq 3.00$, with the irregularity least severe in the laminar regime ($Re = 56$) and most severe in the turbulent regime ($Re = 9,500$).

TABLE II: Comparison of predicted Strouhal number, St, for varying M_∞.

M_∞	RPT	CFD[43]
0.01	0.207	0.212
0.1	0.174	
0.2	0.239	0.208
0.3	0.228	0.206
0.4	0.228	0.203
0.5	0.228	0.198

Figure 9a shows the one-dimensional energy spectra of the crossflow velocity in a cylinder wake for varying M_∞, $Re = 3,900$, and $\gamma = 1.4$ at $(\tilde{x}/D, \tilde{y}/D) = (3.00, 0.56)$. These are wavenumber spectra[5] produced from 829,250 samples that were obtained over a duration of 11.28s while advancing downstream at V_∞ from each sampled location where the theoretical flow was frozen at $t_0 = 75,500R/V_\infty$. The Fast-Fourier Transform (FFT) was used to compute the spectra. The frequency is non-dimensionalized by the vortex shedding frequency, f_{VS}. This Strouhal frequency and its first harmonic (at $\sim 3f_{VS}$) are distinctly visible in the $M_\infty < 10^{-5}$ spectrum in which there are decades of wavenumber where the slope of the spectrum is $-5/3$, signifying the inertial range of turbulence in excellent agreement with experimental and CFD results in the incompressible regime[43] (figure 4, p.7). The inertial range of the turbulence is disrupted by compressibility effects as M_∞ increases, introducing some background noise into the spectra that slightly conceals the first harmonic at $\sim 3f_{VS}$. This is in contrast to the CFD energy spectra under similar Re and M_∞ conditions but a different vertical wake location on the center line (figure 9b[43]) in which both the inertial range and first harmonic at $3f_{VS}$ are distinctively discernible across the sampled Mach number range. As M_∞ increases, a corresponding change in the fluid viscosity that is appropriately computed via a coupling of the governing equations, including the energy equation, and Sutherland's law maintains the energy cascade in the CFD as opposed to the RPT model. Figure 9a is not evaluated on the wake center line because the finite velocity jump on the rear axis of the cylinder in RPT present some difficulty for spectra analysis at that location[5]. However, the spectra analyses in figure 10, with flow conditions similar to that of figure 9a, are at equivalent $(\tilde{x}/D, \tilde{y}/D) = (0.69, 0.69)$ to CFD results[43] (figure 22, p.14), giving a more direct comparison and the opportunity to assess the behavior of the shear layer in RPT under compressibility effects. The streamwise velocity spectra (not shown here) are much noisier and present greater difficulty in reading the Strouhal frequency off the spectra as M_∞ increases. Thus, in Table II, only the RPT Strouhal numbers for $M_\infty \leq 0.01$ were read off the spectra of the streamwise velocity. The crossflow velocity oscillates at a dominant frequency that is higher than the CFD and Nagata et al.'s[1] (figure 13, p.15) experimental results at the corresponding M_∞. The relevant part of Nagata et al.'s[1] (figure 13, p.15) experimental results to the current discussion are at a close $Re = 4,000$, contrary to the RPT and CFD results that are at $Re = 3,900$. However, one of the general trends in the RPT predictions that agrees with both CFD and the experimental results is that compressibility has only a marginal effect on the Strouhal number for $0.2 \leq M_\infty \leq 0.5$. The shape of the spectra remains the same in this Mach range and markedly different for $M_\infty < 10^{-5}$. From $M_\infty < 10^{-5}$, the energy increases with M_∞, but remains unchanged in the range $0.2 \leq M_\infty \leq 0.5$, contrary to CFD[43]. However, the second harmonic shifts from $\sim 3f_{VS}$ to $\sim 2f_{VS}$ as the Mach number increases from $M_\infty < 10^{-5}$ to the $0.2 \leq M_\infty \leq 0.5$ range in an excellent agreement with CFD[43]. The harmonic at $\sim 3f_{VS}$ is

AIP Publishing Physics of Fluids ACCEPTED MANUSCRIPT
This is the author's peer reviewed, accepted manuscript. However, the online version of record will be different from this version once it has been copyedited and typeset.
PLEASE CITE THIS ARTICLE AS DOI: 10.1063/5.0332888

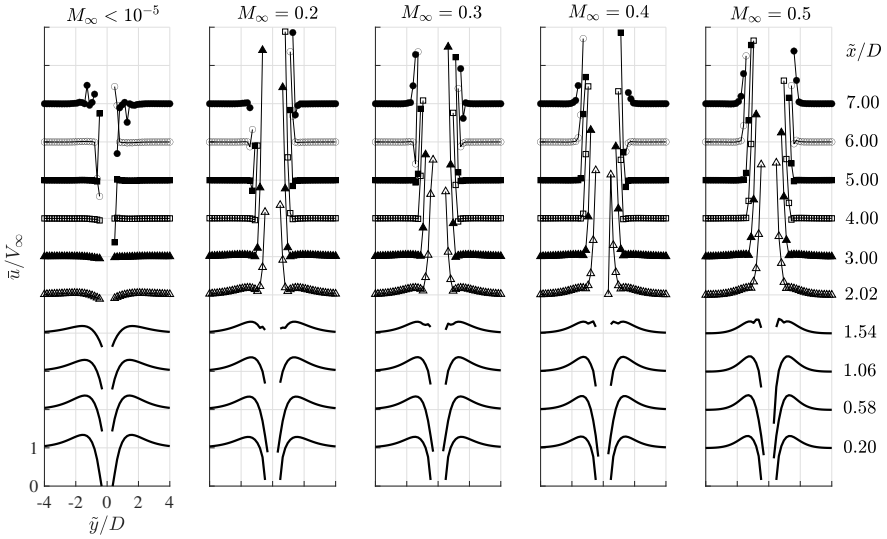


FIG. 6: Time-averaged streamwise velocity in a cylinder wake for varying M_∞ at $Re = 3,900$.

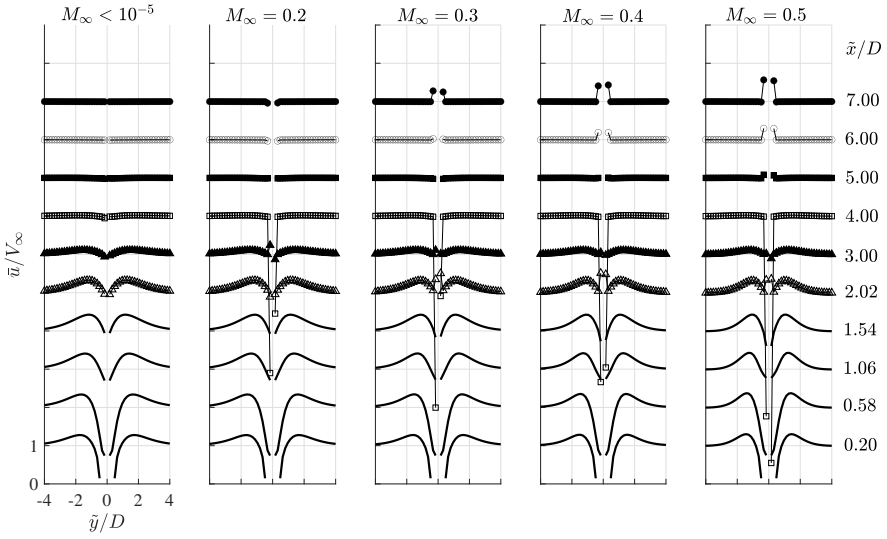


FIG. 7: Time-averaged streamwise velocity in a cylinder wake for varying M_∞ at $Re = 56$.

AIP Publishing Physics of Fluids ACCEPTED MANUSCRIPT
This is the author's peer reviewed, accepted manuscript. However, the online version of record will be different from this version once it has been copyedited and typeset.
PLEASE CITE THIS ARTICLE AS DOI: 10.1063/5.0332888

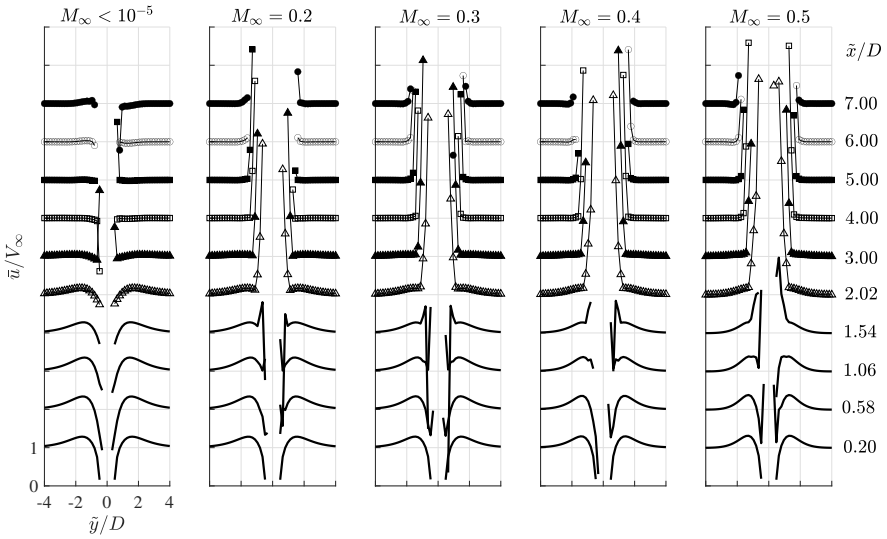


FIG. 8: Time-averaged streamwise velocity in a cylinder wake for varying M_∞ at $Re = 9,500$.

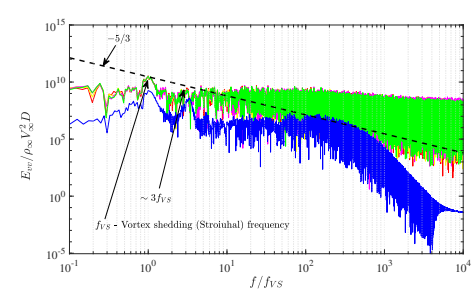
reduced in energy but becomes part of a system of pseudo-peaks that includes the shear layer frequency, f_{SL}, at $\sim 7 f_{VS}$ (in figure 10a). This value of shear layer frequency is about a tenth of its value for $M_\infty < 10^{-5}$ (in figure 10b). This suggests that compressibility in RPT suppresses shear layer instability, favoring lower frequency oscillations as observed in both experimental[1] and CFD[43] investigations.

The effect of the change in γ on the compressible flow at this location is also explored and presented in figure 11. The energy spectra of the streamwise velocity for three values of $\gamma = 1.4$ (diatomic gas), 1.67 (monoatomic gas), and 3.00 (magnetized plasma with a one degree of freedom[67,68]) are presented for $Re = 3,900$ and $M_\infty = 0.5$. The energy of the spectra reduces as the degree of freedom reduces and γ rises. The shape of the spectra also changes as the range of wavenumbers for which the slope is $-5/3$ shrinks in the process, gradually energizing higher frequencies. This suggests that RPT captures the exchange of energy between kinetic and internal energy modes.

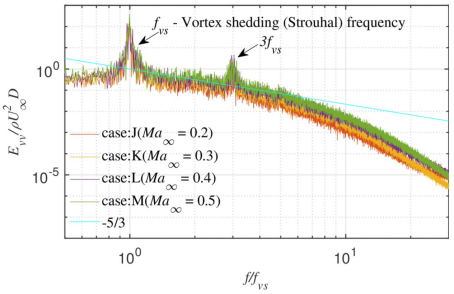
When the conditions in figure 11 are maintained at $\gamma = 3.0$ but the viscosity is varied, more drastic changes to the spectra are observed in figure 12. From $\nu = 1.46069 \times 10^{-5} m^2/s$, increasing the viscosity by three orders of magnitude depletes the energy on all scales and moves the spectrum to the low-frequency range with no frequency fall-off characteristics. However, the spectrum moves into the very high frequency dissipation range with a much steeper fall-off slope than the inertial range while at sufficiently lower energies on all scales when the viscosity is decreased by three orders of magnitude to $\nu = 1.46069 \times 10^{-8} m^2/s$. These arbitrarily chosen values of viscosity demonstrate how RPT wake characteristics are affected by the freestream temperature dependent properties.

The instantaneous flow fields presented in figures 13 and 14 show the RPT streamline contours at $Re = 3,900$, $t = 5,000 R/V_\infty$, $\nu = 1.46069 \times 10^{-8} m^2/s$, and $\gamma = 3.0$ for $10^{-5} > M_\infty \leq 0.99$ in the cylinder reference frame[5]. At $M_\infty < 10^{-5}$, the large scale staggered von Kármán vortices are distinctively discernible and break off into the wake at some distance from the cylinder after the recirculation zone. This is why the spectral peaks at the Strouhal frequency and its harmonics are sharp in the energy spectra plot. As the Mach number rises to $M_\infty = 0.5$, compressibility effects introduce energetic smaller scale structures that almost overwhelm the periodicity of the wake, bringing the pinch-off location[1] of the von Kármán vortices closer to the cylinder. Migration of the pinch-off location towards the cylinder with compressibility effects has also been experimentally observed at $Re = 4,000$[1]. By $M_\infty = 0.5$, the width of the wake begins to grow with the distance from the cylinder as the wake fans out. The curvature of the cylinder accelerates the flow over the crests so that the streamlines begin to depress towards the cylinder at $M_\infty = 0.6$. As M_∞ progressively increases, the acceleration effect becomes stronger until pockets of locally supersonic flow bounded by Mach waves appear above the recirculation region by $M_\infty = 0.8$. Initially, the bases of these pockets are almost flat and inclined away from the freestream direction. This inclination further expands the local supersonic flow in the interior. The expanded flow recompresses when it hits the upward slope of the wake, forming a rear shock. As M_∞ gradually approaches one (1), the pockets grow in extent. The

ACCEPTED MANUSCRIPT
Physics of Fluids
AIP Publishing
This is the author's peer reviewed, accepted manuscript. However, the online version of record will be different from this version once it has been copyedited and typeset.
PLEASE CITE THIS ARTICLE AS DOI: 10.1063/5.0332888

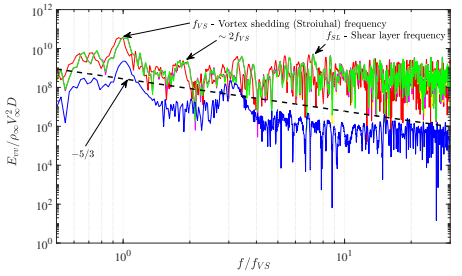


(a) $(\tilde{x}/D,\tilde{y}/D) = (3.00, 0.56)$: $M_\infty < 10^{-5}$ (–); $M_\infty = 0.2$ (–); $M_\infty = 0.3$ (–); $M_\infty = 0.4$ (–); $M_\infty = 0.5$ (–)

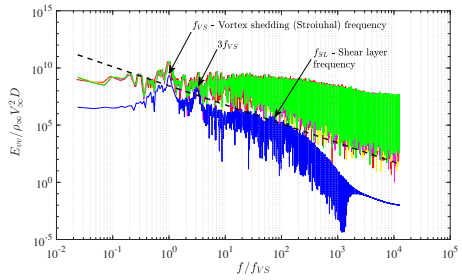


(b) $(x/D,y/D) = (3.00, 0)$[43]. Reproduced from Kuiju Xue, Qinling Li, and Liangyu Zhao, Physics of Fluids, 36, 085165 (2024), with the permission of AIP Publishing.

FIG. 9: Energy spectra of the crossflow velocity in a cylinder wake for varying M_∞ at $Re = 3,900$ for RPT (a) and CFD[43] (b).



(a)



(b)

FIG. 10: Energy spectra of the crossflow velocity in a cylinder wake for varying M_∞ at $Re = 3,900$ and $(\tilde{x}/D,\tilde{y}/D) = (0.69, 0.69)$.$M_\infty < 10^{-5}$ (–); $M_\infty = 0.2$ (–); $M_\infty = 0.3$ (–); $M_\infty = 0.4$ (–); $M_\infty = 0.5$ (–),

gaps between their bases and the cylinder crests close. The bases become wavy with a trough-crest-trough outline. Start-

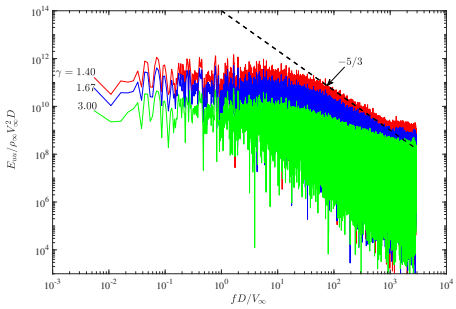


FIG. 11: Energy spectra of the streamwise velocity in a cylinder wake for varying γ at $Re = 3,900$, $M_\infty = 0.5$ and $(\tilde{x}/D,\tilde{y}/D) = (0.69, 0.69)$.

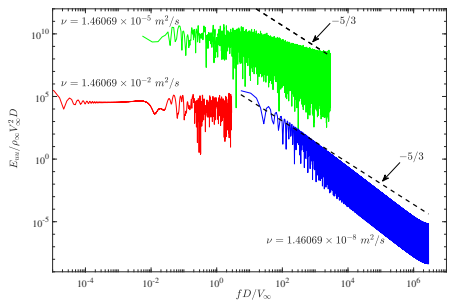


FIG. 12: Energy spectra of the streamwise velocity in a cylinder wake for varying ν at $Re = 3,900$, $M_\infty = 0.5$, $\gamma = 3.0$ and $(\tilde{x}/D,\tilde{y}/D) = (0.69, 0.69)$.

AIP Publishing Physics of Fluids ACCEPTED MANUSCRIPT
This is the author's peer reviewed, accepted manuscript. However, the online version of record will be different from this version once it has been copyedited and typeset.
PLEASE CITE THIS ARTICLE AS DOI: 10.1063/5.0332888

ing from the upstream trough, the upward slope of the base's crest turns the supersonic flow into itself, forming a series of compression waves. These waves coalesce into internal bow shocks at $M_\infty = 0.9$. The shocks lose their strength towards $M_\infty = 0.99$. However, the downward slope of the base's crest turns the flow away from itself. Consequently, the flow is expanded through a series of expansion waves towards the rear bow shocks that are formed as the upward slope of the wake recompresses the flow. The rear bow shocks interact with the recirculation region in the wake, coming together to form a complex system of lamda (λ) shocks[8] by $M_\infty = 0.99$ as shown in figure 15. This figure has striking similarities to a CFD result under similar conditions ($Re = 3{,}900$ and $M_\infty = 0.9$)[8] (figure 3, p. 7) and an experimental flow visualization at an unknown Re but $M_\infty = 0.98$[72] (figure 222, p. 131). However, there are notable differences including the displacement of the supersonic region from the cylinder and the shortened separated shear layers compared to experiments and CFD.

The physics of the supersonic pocket can be modified by varying some parameters. The strength of its internal shock is proportional to the radius of the cylinder as illustrated in figure 16. The internal shock can be smoothed out by increasing the viscosity as shown in figure 17. Figure 18 shows that the pocket can be delayed with a decrease in γ. Reducing Re to $1{,}000$ strengthens the internal shock and positions the base of the pocket on the cylinder. However, increasing it to $9{,}500$ strengthens the internal shock to a normal shock wave without dislocating the base of the pocket downward to the cylinder. In addition, this introduces a much more complex interaction downstream of the internal shock, as depicted in figure 19. Some of these changes, including the elongation of the separated shear layers, can also be achieved by varying just the non-dimensional time as figure 20 presents, featuring transient disruptions of flow symmetry in the unsteady flow development.

Figure 21 employs a numerical schlieren technique (using the function $S(x,y)$[28,73] defined in Eq. 25) to visualize the instantaneous density gradient field of RPT at $t = 5{,}000R/V_\infty$, $\nu = 1.46069 \times 10^{-8} m^2/s$, $\gamma = 3.0$ and $Re = 3{,}900$ for $M_\infty =$ 0.99, 1.01 and 1.35. The density field is evaluated from Eq. 15. Equation 25 contains two adjustable parameters, β and K, whose values were set at 0.95 and 15, respectively. β controls the zero gradient and K regulates the amplification of small gradients[28]. $|\nabla\rho|_{max}$ is the maximum absolute density gradient in the entire flow field. The contour levels are spaced $1/140$ between zero (0) and one (1).

$$S(x,y) = \beta exp\left(-\frac{K|\nabla\rho|}{|\nabla\rho|_{max}}\right) \tag{25}$$

As the free stream reaches a slightly supersonic $M_\infty = 1.01$, the λ-shock system in figure 21a disappears and is replaced by an upstream bow shock at a distance from the cylinder, as shown in figure 21b. The shock detachment distance closes and the bow shock curvature intensifies when $M_\infty = 1.35$ in figure 21c. These observations are in good qualitative agreement with CFD and experimental investigations of the transonic flow field of a cylinder.

To aid in a quantitative assessment, the mean streamwise velocity profiles are evaluated along some of the overlaying grid lines in figure 21 and presented in figures 22 to 25 for the three M_∞. These mean values are the average quantities numerically integrated over the same time period as in figure 4. The wake streamwise velocity profiles at three vertical downstream locations are shown in figure 22. Outlier points still exist on the rear axis and are omitted. At $M_\infty = 0.99$, station $\tilde{x}/D = 2.02$ is upstream of the λ-shock system but cuts through the rear bow shocks. Consequently, there are discontinuities in the velocity profile at $\tilde{y}/D \sim \pm 5$ corresponding to the shock locations where the magnitude of the streamwise velocity is greater than $40V_\infty$. Compared with Lin's[8] (figure 10a, p.13) CFD result at a similar $M_\infty = 0.9$, the rear bow shocks do not feature in the profile at $\tilde{x}/D = 2.00$ (in figure 23) but further downstream at $\tilde{x}/D = 8.00$ (due to the elongated free shear layers) where the general outline of the profile (between the shocks, including the protrusion in the separated shear layer region) and the lateral locations of the discontinuity of the profile at $\tilde{y}/D \sim \pm 5$ are similar to RPT. Whereas station $\tilde{x}/D = 4.00$ is directly downstream of the rear bow shock in the present RPT result, it is an upstream station to the entire shock system in the CFD result. This explains the difference in the RPT and CFD profiles at this station in figure 23. Both stations $\tilde{x}/D = 7.00$ for the RPT and $\tilde{x}/D = 10.00$ for the CFD are sufficiently downstream of the respective shock-systems and have very similar profiles. The RPT velocity profiles at $M_\infty = 1.01$ and 1.35 are similar for all three downstream locations. They are also similar to the profile at $\tilde{x}/D = 7.00$ for $M_\infty = 0.99$.

The streamwise velocity profiles along horizontal locations in the range $0.35 \leq \tilde{y}/D \leq 3$ are shown for the three M_∞ in figures 24 and 25. These locations were chosen for comparison with Li's[8] (figure 9, p.13) CFD results at $M_\infty = 0.9$. Although the CFD results do not include the windward freestream, the present profiles cover the upstream far field and the wake. This is to facilitate a comparison of the complete transonic flow field phenomena as M_∞ is varied. The upstream centerline also has a singular behavior similar to the cylinder rear axis and is therefore left out. In the freestream, the profiles coincide for the three M_∞. As the flow approaches the cylinder, it encounters a weak shock wave at $M_\infty = 1.01$. This is identifiable as discontinuities in the profiles around $\tilde{x}/D = -5$ for $0.35 \leq \tilde{y}/D \leq 1.00$. This discontinuity is more visible at $\tilde{y}/D = 1.00$, while it appears as a kink in the profiles at $\tilde{y}/D = 0.35$ and 0.5 due to the relatively large excursions in the wake velocity variations in the respective figures. The predicted shock detachment distance, δ/D, at $M_\infty = 1.01$ is ~ 4.5, which is consistent with published experimental and computational trends[65] (figure 7, p.7). There is no upstream shock at this location for $M_\infty = 0.99$ and $M_\infty = 1.35$. Moving closer to the cylinder ($-1.74 \geq \tilde{x}/D \geq -4.80$), the profiles remain overlapped for $0.35 \leq \tilde{y}/D \leq 0.5$ because the incident weak shock when $M_\infty = 1.01$ reduces the flow velocity by a negligible amount and the curvature of the cylinder has a minimal effect. However, the situations are different for $1.00 \leq \tilde{y}/D \leq 3.00$. At $\tilde{y}/D = 1.00$, the post shock $M_\infty = 1.01$ flow and the $M_\infty = 0.99$ freestream flow are both subsonic and accelerate to higher velocities by the cylinder curvature.

ACCEPTED MANUSCRIPT
Physics of Fluids
AIP Publishing
This is the author's peer reviewed, accepted manuscript. However, the online version of record will be different from this version once it has been copyedited and typeset.
PLEASE CITE THIS ARTICLE AS DOI: 10.1063/5.0332888

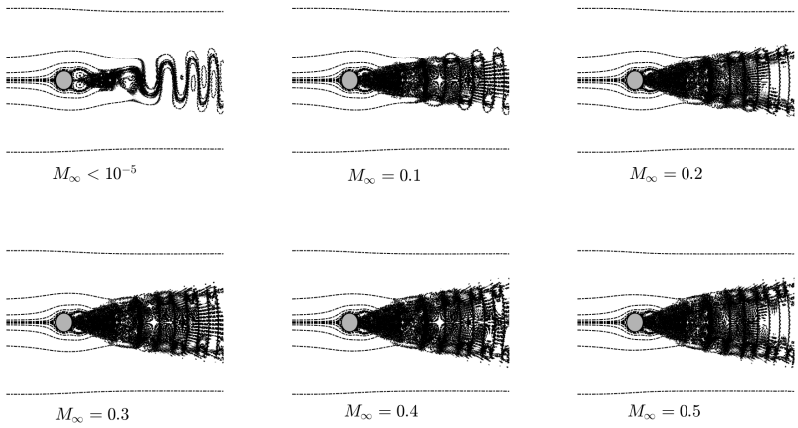


FIG. 13: Streamline for $Re = 3,900$ and $t = 5,000R/V_\infty$,$\nu = 1.46069 \times 10^{-8} m^2/s$, and $\gamma = 3.0$.

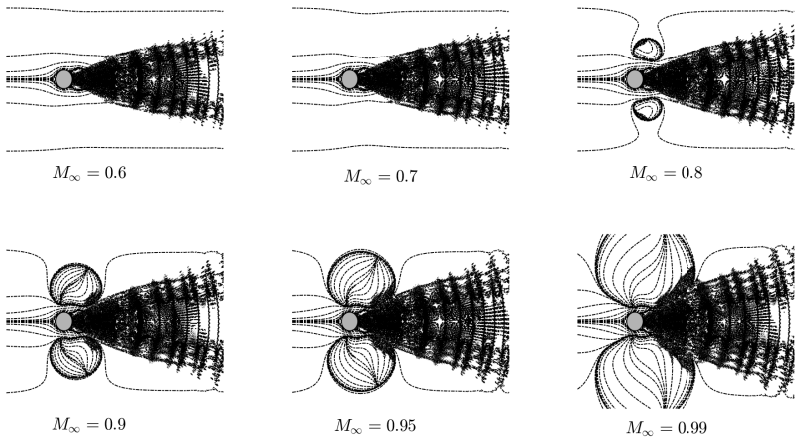


FIG. 14: Streamline for $Re = 3,900$ and $t = 5,000R/V_\infty$,$\nu = 1.46069 \times 10^{-8} m^2/s$, and $\gamma = 3.0$.

The post shock $M_\infty = 1.01$ flow hits the sonic line, and the $M_\infty = 0.99$ freestream encounters the leading shock of the supersonic pocket around $\tilde{x}/D \approx -0.98$. At $\tilde{y}/D = 2.00$ and 3.00, the $M_\infty = 0.99$ freestream continues to expand, crossing the leading shock of the supersonic pocket at $\tilde{x}/D \approx -2.08$ and $\tilde{x}/D \approx -2.42$, respectively. At $\tilde{y}/D = 2.00$ and 3.00, the curvature effect of the cylinder gradually turns the $M_\infty = 1.01$ freestream into itself, compressing and slowing it down to subsonic conditions. This compression happens without a shock. When the subsonic condition is reached, the flow velocity begins to increase as the flow expands around the cylinder.

The $M_\infty = 1.35$ freestream encounters a shock around $\tilde{x}/D \approx -1.7$ and $\delta/D \sim 1.2$. This value of δ/D is lower

ACCEPTED MANUSCRIPT
Physics of Fluids
AIP Publishing
This is the author's peer reviewed, accepted manuscript. However, the online version of record will be different from this version once it has been copyedited and typeset.
PLEASE CITE THIS ARTICLE AS DOI: 10.1063/5.0332888

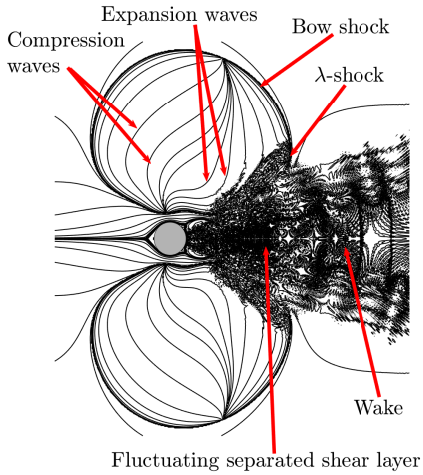


FIG. 15: Streamline for $Re = 3,900$ and $t = 5,000R/V_\infty$, $\gamma = 3.0, \nu = 1.46069 \times 10^{-8} m^2/s$, $M_\infty = 0.99$.

than the computational and experimental results for a gas with $\gamma = 1.4$[65]. However, δ/D has a proportional relationship with γ[74]. So,it is expected that the present results with $\gamma = 3.0$ have a higher value of δ/D. This is due to the breakdown of the one-way coupling of the density field on an incompressible base flow, offering insufficient feedback to the modeled compressible flow field at this supersonic regime. Between $-0.5 \geq \tilde{x}/D \geq -1.7$, the velocity profiles again coincide for $0.35 \leq \tilde{y}/D \leq 0.5$ because the flows are in similar locally subsonic conditions. The $M_\infty = 0.99$ profiles dip for $1.00 \leq \tilde{y}/D \leq 3.00$ due to the re-compression of the local flow by the upward slope of the base of the supersonic pocket. However, the $M_\infty = 1.01$ and 1.35 profiles are increasing under the effect of the cylinder curvature. For $\tilde{x}/D > -0.5$, the three profiles overlap at almost every point except in the very near wake for $\tilde{y}/D = 0.35$ and 0.50. Between $1.00 \leq \tilde{y}/D \leq 3.00$, flows expand at different rates. The $M_\infty = 1.35$ recompresses in the wake without any shocks but compression waves. Re-compression of the $M_\infty = 1.01$ flow occurs through a trailing shock at $\tilde{y}/D = 1.00$, but gradually through compression waves at higher locations. The $M_\infty = 0.99$ flow recompresses in the wake through the λ-shock system for $1.00 \leq \tilde{y}/D \leq 3.00$. At a similar $M_\infty = 0.9$ in Li's[8] (figure 9, p.13) CFD results, the flow also recompresses through shocks for $1.00 \leq \tilde{y}/D \leq 3.00$. However, the RPT flow does not recompress to the freestream in contrast to Li's result. This is likely because the time period is not sufficient to average out the large velocity fluctuations in the wake eddies.

The one-dimensional energy spectra of the streamwise velocity at a far field location in the wake are presented for the three M_∞ in figure 26. These are obtained in a similar way to figure 9a. The spectra are identical across M_∞. The turbulence decays at a rate that is consistent with Kolmogorov's Five-Thirds law. The Strouhal frequency of the incompressible flow, 0.207, is no more dominant. Energy is transferred to a range of frequencies close to 0.3 starting with 0.25. There are peaks at 0.364. These are significant predictions because they agree with experimental[9] and computational[8] trends. In particular, at a similar $M_\infty = 0.9$ and in the far field, the separated shear layers fluctuate at a Strouhal frequency 0.4 in Li's[8] direct numerical simulation (DNS) results. This is very close to the observed peak at 0.364 in the present result at $M_\infty = 0.99$. The Strouhal frequency at 0.2 is also deprived of dominant energy in DNS results. Furthermore, Awasthi et al.[9] experimentally observed that the energy at this hydrodynamic frequency is weaker than the energy at an aeroacoustic shedding frequency of 0.42 in a supersonic cylinder wake. Additionally, the universal Strouhal number is approximately 0.3. These are in agreement with the present observations at a supersonic $M_\infty = 1.35$ where there are dominant shedding frequencies around 0.3 and the spectral peak at 0.364 is within a 13% range of the measured aeroacoustic frequency.

However, the compressible extension of RPT is not a fully predictive tool in strongly transonic/supersonic and highly turbulent conditions but an approximate model with delimited validity. Where the model departs significantly from CFD and experimental data, it is partly because it rests on an isentropic density closure built on an incompressible base flow, employs a constant viscosity, and is without an explicit coupling with the energy equation. In the literature, the one-way coupling of the density field is valid at $M_\infty < 0.3$ where the modest density variations cause minimal or negligible volume dilatation[75]. At higher M_∞, the volume dilation due to these changes is not negligible, and there is a mutual dependence between velocity, density, and pressure[75]. However, in the present analysis it produces qualitatively reliable results in $30 < Re < 10,000$ for $M_\infty \leq 1.01$ possibly because the velocity field is kept divergence-free.

V. CONCLUSION

This article explores the compressible flow field around an impulsively started circular cylinder using RPT. The purpose of the study is an attempt to address some of the limitations of experimental and CFD methods by providing an analytical model to complement these approaches. The research focuses on subsonic compressible and transonic ($M_\infty \leq 1.01$) flow physics in the subcritical regime ($30 < Re < 10,000$), with potential applications in aerospace engineering, space exploration, and astrophysics.

A. Key Findings

1. Compressibility Effects: Compressibility marginally increases vortex enstrophy at low Re, as evidenced by tighter streamlines around vortex centers. At higher Re (e.g., 3,900), compressibility effects are less pronounced in the wake flow stability, with nearly constant

AIP Publishing Physics of Fluids ACCEPTED MANUSCRIPT
This is the author's peer reviewed, accepted manuscript. However, the online version of record will be different from this version once it has been copyedited and typeset.
PLEASE CITE THIS ARTICLE AS DOI: 10.1063/5.0332888

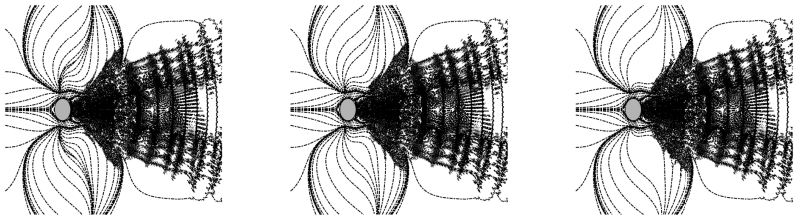


FIG. 16: Streamline for $Re = 3,900$ and $t = 5,000R/V_\infty$,$M_\infty = 0.99$, $\nu = 1.46069 \times 10^{-8} m^2/s$, $\gamma = 3.0$.

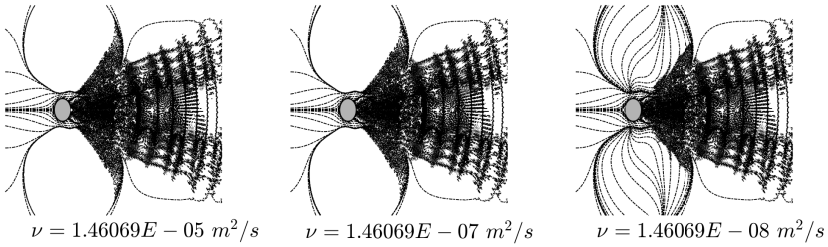


FIG. 17: Streamline for $Re = 3,900$ and $t = 5,000R/V_\infty$,$M_\infty = 0.99$, $\gamma = 3.0$.

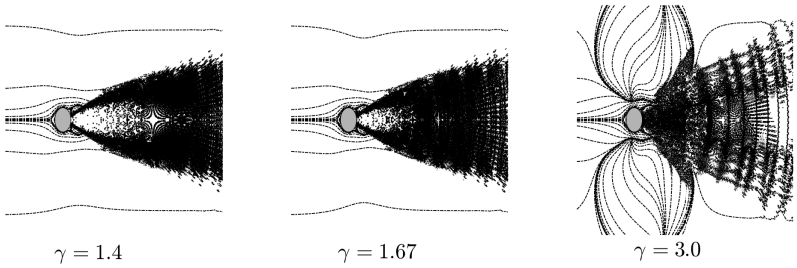


FIG. 18: Streamline for $Re = 3,900$ and $t = 5,000R/V_\infty$,$\nu = 1.46069 \times 10^{-8} m^2/s$, $M_\infty = 0.99$.

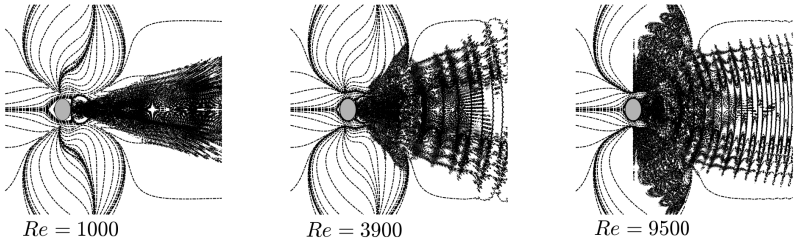


FIG. 19: Streamline for varying Re and $t = 5,000R/V_\infty$,$M_\infty = 0.99$, $\nu = 1.46069 \times 10^{-8} m^2/s$, $\gamma = 3.0$.

ACCEPTED MANUSCRIPT
Physics of Fluids
AIP Publishing
This is the author's peer reviewed, accepted manuscript. However, the online version of record will be different from this version once it has been copyedited and typeset.
PLEASE CITE THIS ARTICLE AS DOI: 10.1063/5.0332888

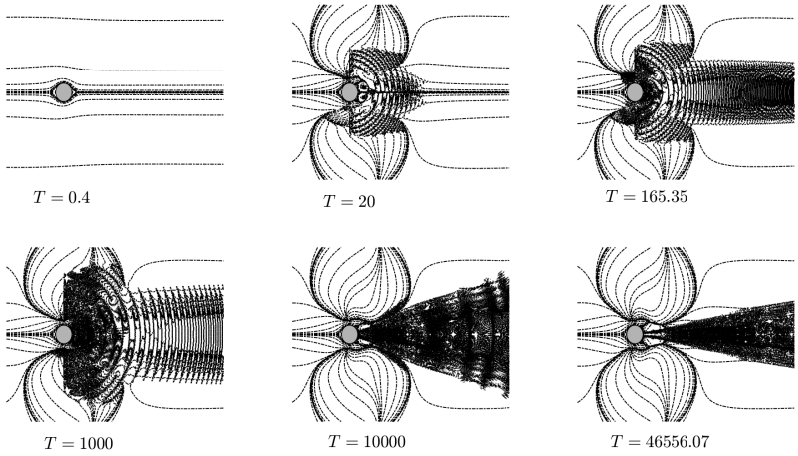


FIG. 20: Streamline for $Re = 3,900$ and $M_\infty = 0.99$, $\nu = 1.46069 \times 10^{-8} m^2/s$, $\gamma = 3.0$. $T = V_\infty t/R$

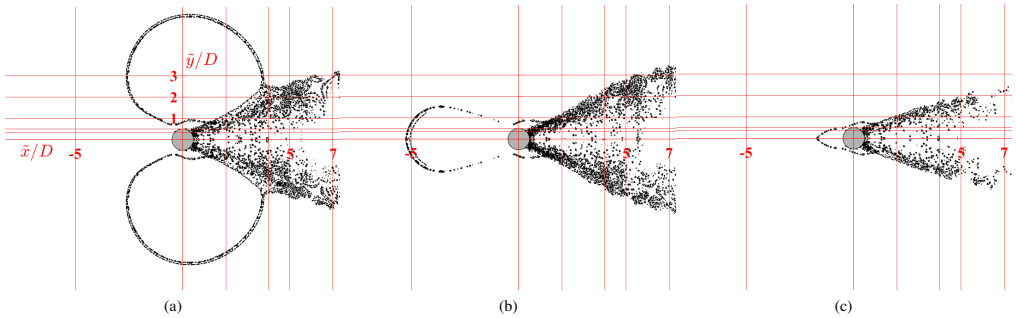


FIG. 21: Density gradient field for $Re = 3,900$, $t = 5,000R/V_\infty$, $\gamma = 3.0$,$\nu = 1.46069 \times 10^{-8} m^2/s$, and (a)$M_\infty = 0.99$ (b)$M_\infty = 1.01$ (c)$M_\infty = 1.35$.

recirculation zone dimensions across varying Mach numbers ($M_\infty \leq 0.5$).

2. Wake Characteristics: Compressibility reduces the velocity deficit in the wake and suppresses shear layer instability, favoring lower frequency oscillations. The recirculation zone length and wake stability are less sensitive to compressibility at $Re = 3,900$ for $M_\infty \leq 0.5$, contrary to CFD results.

3. Strouhal Number: The Strouhal number predictions from RPT show marginal changes for $0.2 \leq M_\infty \leq 0.5$, aligning with experimental and CFD trends. Compressibility introduces energetic smaller-scale structures, disrupting the inertial range of turbulence and altering the energy spectra.

4. Local Supersonic Flow Features: At higher Mach numbers ($M_\infty \geq 0.6$), local supersonic pockets and shock waves appear in the wake, with complex interactions such as λ-shocks and bow shocks forming at $M_\infty = 0.99$ and above. The supersonic pocket's characteristics, such as internal shock strength and location, are influenced by parameters like cylinder radius, viscosity, and specific heat ratio (γ).

5. Energy Spectra: Compressibility effects introduce background noise into energy spectra, reducing the

ACCEPTED MANUSCRIPT
Physics of Fluids
AIP Publishing
This is the author's peer reviewed, accepted manuscript. However, the online version of record will be different from this version once it has been copyedited and typeset.
PLEASE CITE THIS ARTICLE AS DOI: 10.1063/5.0332888

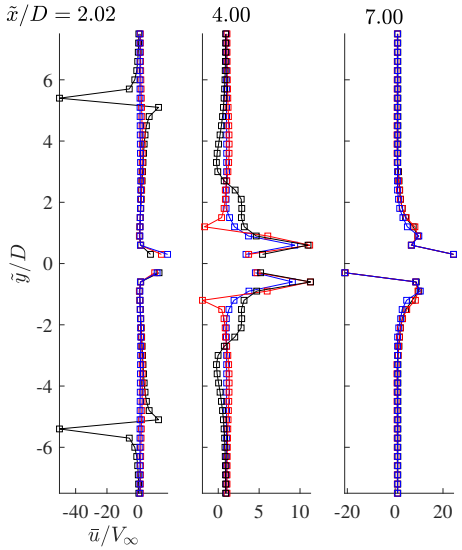


FIG. 22: Mean streamwise velocity profile at three downstream locations for $Re = 3,900$, $\nu = 1.46069 \times 10^{-8} m^2/s$, and $\gamma = 3.0$. $M_\infty = 0.99$ $(-)$; $M_\infty = 1.01$ $(-)$; $M_\infty = 1.35$ $(-)$

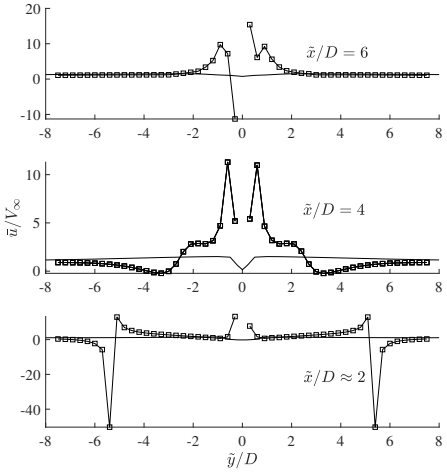


FIG. 23: Comparison of RPT mean streamwise velocity profile at three downstream locations for $Re = 3,900$, $\nu = 1.46069 \times 10^{-8} m^2/s$, and $\gamma = 3.0$ ($M_\infty = 0.99$: $-\square-$) with digitized CFD data[8] ($M_\infty = 0.9$: $-$). Shuai Li, Phys. Rev. Fluids 8, 034603,2025; licensed under a Creative Commons Attribution 4.0 International (CC BY 4.0) license.

dominance of Strouhal frequency and favoring lower frequency oscillations. At supersonic Mach numbers, energy is transferred to higher frequencies, consistent with experimental and computational observations.

B. Conclusions

RPT provides a valuable analytical tool for modeling compressible flow over circular cylinders, capturing key flow features such as wake dynamics, vortex shedding, and compressibility effects. Although RPT aligns with the experimental and CFD results in some aspects, there are discrepancies, particularly in the wake flow stability and the dimensions of the recirculation zone at higher Re and M_∞.

The study highlights the potential of RPT to complement experimental and numerical methods, offering insights into compressible flow physics for applications in aerospace and astrophysics. Future work could focus on addressing the limitations of RPT, such as its inability to fully replicate the elongated free shear layers and wake recompression observed in experiments and CFD. These limitations stem from the use of an isentropic density closure on an incompressible base flow, the application of constant viscosity, and the lack of an explicit feedback from the energy equation. In addition, quantitative analysis of the pressure field and surface quantities, including base pressure and drag, is the subject of further publications. Analysis of the pressure and vorticity distribution in the flow field will aid in assessing the entropy production and the physical credibility of detailed shock predictions. More in-depth quantitative comparisons of key quantities, including recirculation length, Strouhal number, and shock standoff distance, are also in the direction of future analysis.

This research contributes to understanding compressible flows over bluff bodies and provides a foundation for further exploration of refined analytical models in fluid dynamics.

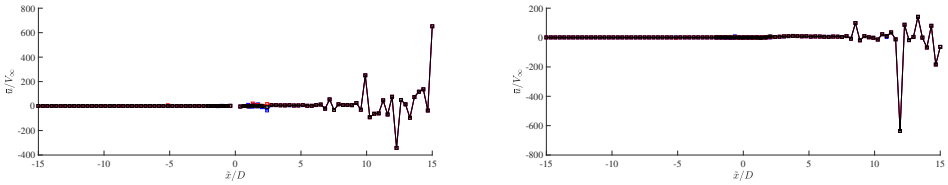
ACKNOWLEDGMENTS

This work is based on Ph.D. research supervised by Professor Marilyn J. Smith and funded by Kwara State University, Malete, Nigeria. The premise of the research was first presented at 2018 AIAA SciTech Forum (AIAA 2018-1288).

DATA AVAILABILITY STATEMENT

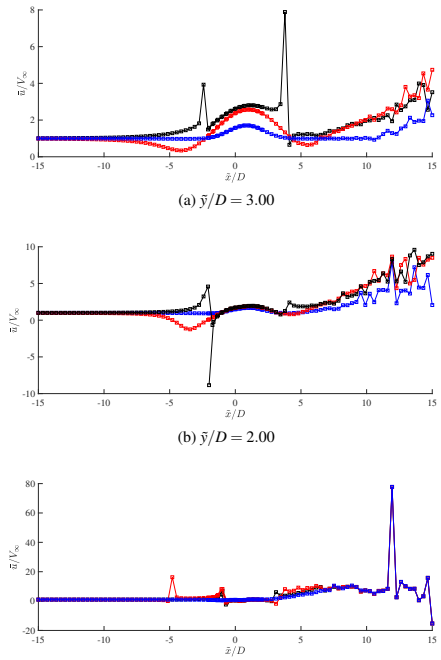
Data that support the findings of this study are available within the article.

ACCEPTED MANUSCRIPT
Physics of Fluids
AIP Publishing
This is the author's peer reviewed, accepted manuscript. However, the online version of record will be different from this version once it has been copyedited and typeset.
PLEASE CITE THIS ARTICLE AS DOI: 10.1063/5.0332888



(a) $\bar{y}/D = 0.35$ (b) $\bar{y}/D = 0.50$

FIG. 24: Mean streamwise velocity in a cylinder flow at vertical locations for $Re = 3,900$, $\gamma = 3.0$,$\nu = 1.46069 \times 10^{-5} m^2/s$, and varying M_∞. $M_\infty = 0.99$ $(-)$, $M_\infty = 1.01$ $(-)$, $M_\infty = 1.35$ $(-)$.



(a) $\bar{y}/D = 3.00$

(b) $\bar{y}/D = 2.00$

(c) $\bar{y}/D = 1.00$

FIG. 25: Mean streamwise velocity in a cylinder flow at vertical locations for $Re = 3,900$, $\gamma = 3.0$,$\nu = 1.46069 \times 10^{-5} m^2/s$, and varying M_∞. $M_\infty = 0.99$ $(-)$, $M_\infty = 1.01$ $(-)$, $M_\infty = 1.35$ $(-)$.

CONFLICT OF INTEREST

The authors have no conflicts to disclose.

Appendix A: Satisfying NSE

Equation 5 highlights the role of ω in incompressible NSE. The velocity field $\mathbf{V} = \nabla\phi$ associated with a classical velocity potential, ϕ, is irrotational and satisfies Eq. 5 identically[55]. However, the velocity field $\mathbf{V} = \nabla \times (\psi_{vis}\hat{\mathbf{e}}_z)$ is rotational and cannot identically satisfy Eq. 5. $\tilde{\kappa}$ is a quasi-potential stream function that satisfies Eq. 5[5,53]. $\tilde{\kappa}$ is derived by resolving ψ_{vis} in the Cartesian wind coordinate system as follow.

The cylindrical polar coordinate variables are related to the Cartesian x-y geometric axes as

$$r = \sqrt{x^2 + y^2} \qquad \theta = \arctan(y,x) \ .$$

This is illustrated in figure 27. There are at least 360 other orientations of the $\tilde{x}$-$\bar{y}$ (wind) axes that correlate with the same cylindrical polar coordinates in figure 27. These correspond to successive units of θ. For a principal axis of the flow, the wind axes in ψ_{vis} are rotated such that

$$\theta = \arctan(x,y) \ , \tag{A1}$$

and the negative $\tilde{x}$-axis is coincident with the positive y-axis. Thus, ψ_{vis} becomes $\tilde{\kappa}$ that is a quasi-potential function in the principal axis. $\tilde{\kappa}$ is summarized in table III. Table III also compares $\tilde{\kappa}$ with ϕ and a generic stream function, ψ. This is illustrated in figures 28 - 31 that present plots of the level sets of the three functions and their velocity fields for the inviscid non-lifting cylinder flow[53,55].

In figures 28a and 28b, the negative x-axis is coincident with the negative $\tilde{x}$-axis, and the freestream flow is parallel to them. However, the freestream flow approaches from the positive y-axis in figure 28c. The streamlines and the potential lines in figures 28a and 28b respectively are orthogonal. However, they describe the same velocity field. Whereas ψ is differentiated in a perpendicular direction to a flow to obtain the velocity components in figure 29, ϕ is differentiated in the flow direction to obtain the same velocity components in figure 30. Thus, ϕ results in an irrotational flow, and ψ does not[55].

In the cylindrical polar coordinate system, the velocity components are obtained from $\tilde{\kappa}$ in a similar way to ψ as depicted in figures31a and 31b. However, in the Cartesian wind coordinate system, $\tilde{\kappa}$ is defined on the principal axes for

ACCEPTED MANUSCRIPT
Physics of Fluids
AIP Publishing
This is the author's peer reviewed, accepted manuscript. However, the online version of record will be different from this version once it has been copyedited and typeset.
PLEASE CITE THIS ARTICLE AS DOI: 10.1063/5.0332888

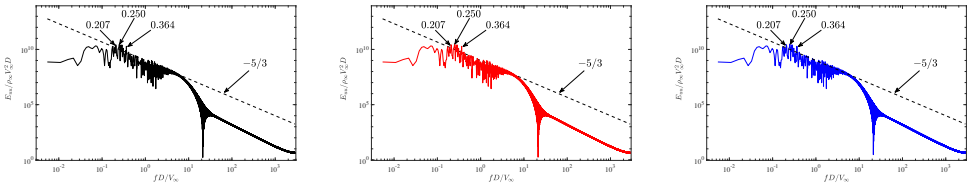


FIG. 26: Energy spectra of the streamwise velocity in a cylinder wake at $(\tilde{x}/D, \tilde{y}/D) = (32, 0.69)$ for $Re = 3,900$, $\gamma = 3.0, \nu = 1.46069 \times 10^{-5} m^2/s$, and (a)$M_\infty = 0.99$ (b)$M_\infty = 1.01$ (c)$M_\infty = 1.35$.

TABLE III: Properties of the $\tilde{\kappa}$ in comparison to ϕ and ψ.

	ϕ	$\tilde{\kappa}$	ψ
V_r	$\frac{\partial \phi}{\partial r}$	$\frac{1}{r}\frac{\partial \tilde{\kappa}}{\partial \theta}$	$\frac{1}{r}\frac{\partial \psi}{\partial \theta}$
V_θ	$\frac{1}{r}\frac{\partial \phi}{\partial \theta}$	$-\frac{\partial \tilde{\kappa}}{\partial r}$	$-\frac{\partial \psi}{\partial r}$
V_z	$\frac{\partial \phi}{\partial z}$	$\frac{\partial \tilde{\kappa}}{\partial z}$	–
V_x	$\frac{\partial \phi}{\partial x}$	$\frac{\partial \tilde{\kappa}}{\partial x}$	$\frac{\partial \psi}{\partial y}$
V_y	$\frac{\partial \phi}{\partial y}$	$\frac{\partial \tilde{\kappa}}{\partial y}$	$-\frac{\partial \psi}{\partial x}$
V_r	$V_x \cos\theta + V_y \sin\theta$	$-V_x \sin\theta + V_y \cos\theta$	$V_x \cos\theta + V_y \sin\theta$
V_θ	$-V_x \sin\theta + V_y \cos\theta$	$-\left(V_x \cos\theta + V_y \sin\theta\right)$	$-V_x \sin\theta + V_y \cos\theta$
V_z	$-(V_x \sin\theta - V_y \cos\theta)\cos\varphi$	$-\left(V_x \cos\theta + V_y \sin\theta\right)\cos\varphi$	–

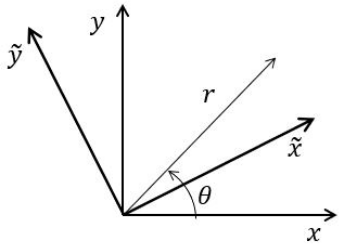


FIG. 27: The relationship between cylindrical polar and Cartesian coordinate systems in ψ_{vis}[53]. Reprinted from "A Closed-Form Analytical Solution to the Complete Three-Dimensional Unsteady Compressible Navier-Stokes Equations", by Taofiq Omoniyi Amoloye, 2022, Research Square (DOI:https://doi.org/10.21203/rs.3.rs-1157529/v1). CC-BY 4.0.

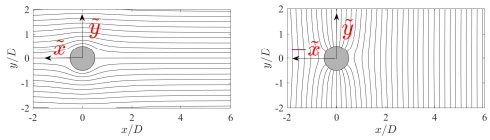
a viscous rotational flow about which ω is identically zero[62] (pp. 57-58). These axes coincide with the wind axes, and the negative principal x-axis points into the incident flow. $\tilde{\kappa}$ is a potential function in these axes, and its velocity components are obtained as

$$x = r\cos\theta \quad y = r\sin\theta \quad z = r\cos\varphi$$

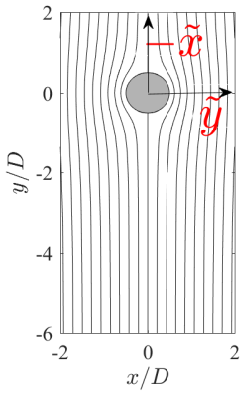
$$V_{\tilde{x}} = \frac{\partial \tilde{\kappa}}{\partial x} = \frac{\partial \tilde{\kappa}}{\partial r}\frac{\partial r}{\partial x} + \frac{\partial \tilde{\kappa}}{r\partial \theta}\frac{r\partial \theta}{\partial x} = -V_\theta \cos\theta - V_r \sin\theta$$
$$V_{\tilde{y}} = \frac{\partial \tilde{\kappa}}{\partial y} = \frac{\partial \tilde{\kappa}}{\partial r}\frac{\partial r}{\partial y} + \frac{\partial \tilde{\kappa}}{r\partial \theta}\frac{r\partial \theta}{\partial y} = -V_\theta \sin\theta + V_r \cos\theta$$
$$V_z = \frac{\partial \tilde{\kappa}}{\partial z} = \frac{\partial \tilde{\kappa}}{\partial r}\frac{\partial r}{\partial z} = -V_\theta \cos\varphi \tag{A2}$$

These are illustrated in figures31c and 31d for the $z = 0$ plane. The positive z-axis extends out of the page. Figure 32 shows that the radial velocity vanishes at the surface because the surface is impermeable.

ACCEPTED MANUSCRIPT
Physics of Fluids
AIP Publishing
This is the author's peer reviewed, accepted manuscript. However, the online version of record will be different from this version once it has been copyedited and typeset.
PLEASE CITE THIS ARTICLE AS DOI: 10.1063/5.0332888



(a) $\psi = r\sin\theta\left(1-\frac{R^2}{r^2}\right)$ (b) $\phi = r\cos\theta\left(1+\frac{R^2}{r^2}\right)$

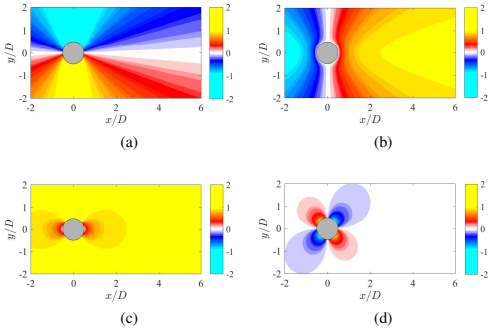


(c) $\tilde{\kappa} = r\sin\left(\arctan\left(r\cos\theta, r\sin\theta\right)\right)\left(1-\frac{R^2}{r^2}\right)$

FIG. 28: A visual comparison of ψ (a), ϕ (b) and $\tilde{\kappa}$ (c) for a cylinder non-lifting flow[53]. Reprinted from "A Closed-Form Analytical Solution to the Complete Three-Dimensional Unsteady Compressible Navier-Stokes Equations", by Taofiq Omoniyi Amoloye, 2022, Research Square (DOI:`https://doi.org/10.21203/rs.3.rs-1157529/v1`). CC-BY 4.0.

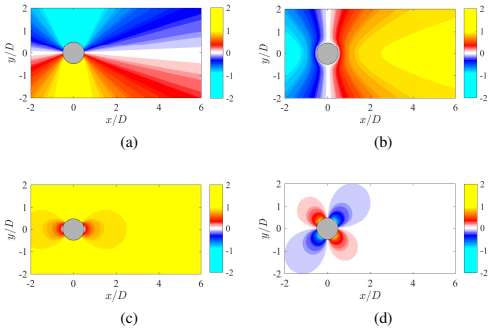
The ω components in the principal axes are computed as

$$\begin{aligned}\frac{\partial V_{\tilde{x}}}{\partial z} &= \frac{\partial^2 \tilde{\kappa}}{\partial z \partial x} \\ &= \frac{\partial}{\partial z}\left(\frac{\partial \tilde{\kappa}}{\partial r}\frac{\partial r}{\partial x} + \frac{\partial \tilde{\kappa}}{r\partial\theta}\frac{r\partial\theta}{\partial x}\right) \\ &= \left(\frac{\partial^2 \tilde{\kappa}}{\partial r^2}\frac{\partial r}{\partial x} + \frac{\partial^2 \tilde{\kappa}}{r\partial r\partial\theta}\frac{r\partial\theta}{\partial x}\right)\frac{\partial r}{\partial z} \\ &= -\left(\frac{\partial V_\theta}{\partial r}\cos\theta + \frac{\partial V_r}{\partial r}\sin\theta\right)\cos\varphi\ ,\end{aligned} \tag{A3}$$



(a) (b) (c) (d)

FIG. 29: An illustration of the non-dimensional planar velocity field of ψ in the inviscid non-lifting cylinder flow. (a) $V_\theta = -\partial\psi/\partial r$, (b) $V_r = \partial\psi/r\partial\theta$, (c) $V_x = \partial\psi/\partial y$ and (d) $V_y = -\partial\psi/\partial x$[53]. Reprinted from "A Closed-Form Analytical Solution to the Complete Three-Dimensional Unsteady Compressible Navier-Stokes Equations", by Taofiq Omoniyi Amoloye, 2022, Research Square (DOI:`https://doi.org/10.21203/rs.3.rs-1157529/v1`). CC-BY 4.0.



(a) (b) (c) (d)

FIG. 30: An illustration of the non-dimensional planar velocity field of ϕ in the inviscid non-lifting cylinder flow. (a) $V_\theta = \partial\phi/r\partial\theta$, (b) $V_r = \partial\phi/\partial r$, (c) $V_x = \partial\phi/\partial x$ and (d) $V_y = \partial\phi/\partial y$[53]. Reprinted from "A Closed-Form Analytical Solution to the Complete Three-Dimensional Unsteady Compressible Navier-Stokes Equations", by Taofiq Omoniyi Amoloye, 2022, Research Square (DOI:`https://doi.org/10.21203/rs.3.rs-1157529/v1`). CC-BY 4.0.

ACCEPTED MANUSCRIPT
Physics of Fluids
AIP Publishing
This is the author's peer reviewed, accepted manuscript. However, the online version of record will be different from this version once it has been copyedited and typeset.
PLEASE CITE THIS ARTICLE AS DOI: 10.1063/5.0332888

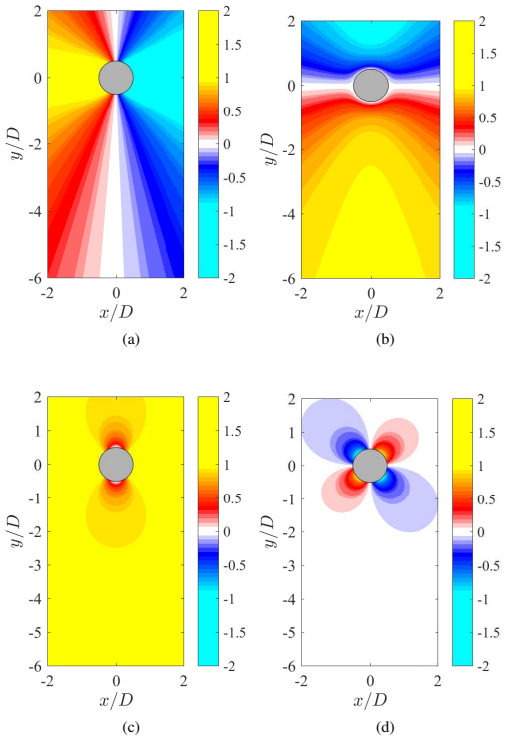


FIG. 31: An illustration of the non-dimensional planar velocity field of $\tilde{\kappa}$ in the inviscid non-lifting cylinder flow. (a) $V_\theta = -\partial\tilde{\kappa}/\partial r$, (b) $V_r = \partial\tilde{\kappa}/r\partial\theta$, (c) $V_x = \partial\tilde{\kappa}/\partial x$ and (d) $V_y = \partial\tilde{\kappa}/\partial y$[53]. Reprinted from "A Closed-Form Analytical Solution to the Complete Three-Dimensional Unsteady Compressible Navier-Stokes Equations", by Taofiq Omoniyi Amoloye, 2022, Research Square (DOI:`https://doi.org/10.21203/rs.3.rs-1157529/v1`). CC-BY 4.0.

$$
\begin{aligned}
\frac{\partial V_{\bar{y}}}{\partial z} &= \frac{\partial^2\tilde{\kappa}}{\partial z\partial y} \\
&= \frac{\partial}{\partial z}\left(\frac{\partial\tilde{\kappa}}{\partial r}\frac{\partial r}{\partial y} + \frac{\partial\tilde{\kappa}}{r\partial\theta}\frac{r\partial\theta}{\partial y}\right) \\
&= \left(\frac{\partial^2\tilde{\kappa}}{\partial r^2}\frac{\partial r}{\partial y} + \frac{\partial^2\tilde{\kappa}}{r\partial r\partial\theta}\frac{r\partial\theta}{\partial y}\right)\frac{\partial r}{\partial z} \\
&= -\left(\frac{\partial V_\theta}{\partial r}\sin\theta - \frac{\partial V_r}{\partial r}\cos\theta\right)\cos\varphi\ ,
\end{aligned}
\tag{A4}
$$

$$
\begin{aligned}
\frac{\partial V_z}{\partial x} &= \frac{\partial^2\tilde{\kappa}}{\partial x\partial z} \\
&= \frac{\partial}{\partial x}\left(\frac{\partial\tilde{\kappa}}{\partial r}\frac{\partial r}{\partial z}\right) \\
&= \frac{\partial^2\tilde{\kappa}}{\partial r^2}\frac{\partial r}{\partial x}\frac{\partial r}{\partial z} + \frac{\partial^2\tilde{\kappa}}{r\partial\theta\partial r}\frac{r\partial\theta}{\partial x}\frac{\partial r}{\partial z} \\
&= -\left(\frac{\partial V_\theta}{\partial r}\cos\theta + \frac{\partial V_r}{\partial r}\sin\theta\right)\cos\varphi\ ,
\end{aligned}
\tag{A5}
$$

ACCEPTED MANUSCRIPT
Physics of Fluids
AIP Publishing
This is the author's peer reviewed, accepted manuscript. However, the online version of record will be different from this version once it has been copyedited and typeset.
PLEASE CITE THIS ARTICLE AS DOI: 10.1063/5.0332888

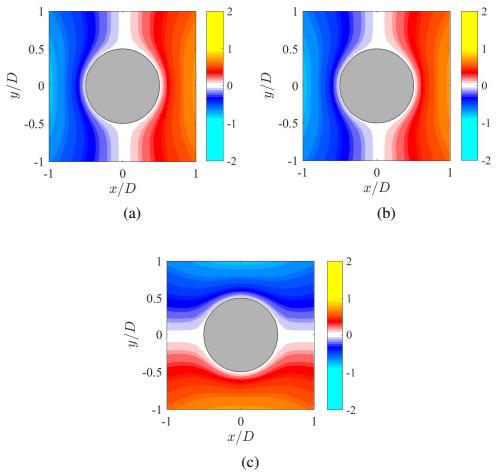


FIG. 32: A zoomed-in view of the radial velocity field. (a) $V_r = \partial\psi/r\partial\theta$, (b) $V_r = \partial\phi/\partial r$ and (c) $V_r = \partial\tilde{\kappa}/r\partial\theta$[53]. Reprinted from "A Closed-Form Analytical Solution to the Complete Three-Dimensional Unsteady Compressible Navier-Stokes Equations", by Taofiq Omoniyi Amoloye, 2022, Research Square (DOI:`https://doi.org/10.21203/rs.3.rs-1157529/v1`). CC-BY 4.0.

$$\begin{aligned}
\frac{\partial V_z}{\partial y} &= \frac{\partial^2\tilde{\kappa}}{\partial y\partial z} \\
&= \frac{\partial}{\partial y}\left(\frac{\partial\tilde{\kappa}}{\partial r}\frac{\partial r}{\partial z}\right) \\
&= \frac{\partial^2\tilde{\kappa}}{\partial r^2}\frac{\partial r}{\partial y}\frac{\partial r}{\partial z} + \frac{\partial^2\tilde{\kappa}}{r\partial\theta\partial r}\frac{r\partial\theta}{\partial y}\frac{\partial r}{\partial z} \\
&= -\left(\frac{\partial V_\theta}{\partial r}\sin\theta - \frac{\partial V_r}{\partial r}\cos\theta\right)\cos\varphi\ ,
\end{aligned} \tag{A6}$$

$$\begin{aligned}
\frac{\partial V_{\tilde{x}}}{\partial y} &= \frac{\partial^2\tilde{\kappa}}{\partial y\partial x} = \frac{\partial}{\partial y}\left(\frac{\partial\tilde{\kappa}}{\partial r}\frac{\partial r}{\partial x} + \frac{\partial\tilde{\kappa}}{r\partial\theta}\frac{r\partial\theta}{\partial x}\right) \\
&= \left(\frac{\partial^2\tilde{\kappa}}{\partial r^2}\frac{\partial r}{\partial y} + \frac{\partial^2\tilde{\kappa}}{r\partial r\partial\theta}\frac{r\partial\theta}{\partial y}\right)\frac{\partial r}{\partial x} + \frac{\partial\tilde{\kappa}}{\partial r}\frac{\partial^2 r}{\partial y\partial x} + \left(\frac{\partial^2\tilde{\kappa}}{r\partial r\partial\theta}\frac{\partial r}{\partial y} + \frac{\partial^2\tilde{\kappa}}{r^2\partial\theta^2}\frac{r\partial\theta}{\partial y}\right)\frac{r\partial\theta}{\partial x} + \frac{\partial\tilde{\kappa}}{r^2\partial\theta}\frac{r^2\partial^2\theta}{\partial y\partial x} \\
&= \left(-\frac{\partial V_\theta}{\partial r}\sin\theta\cos\theta + \frac{\partial V_r}{\partial r}\cos^2\theta + \frac{V_\theta}{r}\sin\theta\cos\theta\right) - \frac{\partial V_r}{\partial r}\sin^2\theta - \frac{V_r}{r}(1-2\cos^2\theta) - \frac{\partial V_r}{r\partial\theta}\sin\theta\cos\theta\ ,
\end{aligned} \tag{A7}$$

$$\begin{aligned}
\frac{\partial V_{\tilde{y}}}{\partial x} &= \frac{\partial^2\tilde{\kappa}}{\partial x\partial y} = \frac{\partial}{\partial x}\left(\frac{\partial\tilde{\kappa}}{\partial r}\frac{\partial r}{\partial y} + \frac{\partial\tilde{\kappa}}{r\partial\theta}\frac{r\partial\theta}{\partial y}\right) \\
&= \left(\frac{\partial^2\tilde{\kappa}}{\partial r^2}\frac{\partial r}{\partial x} + \frac{\partial^2\tilde{\kappa}}{r\partial r\partial\theta}\frac{r\partial\theta}{\partial x}\right)\frac{\partial r}{\partial y} + \frac{\partial\tilde{\kappa}}{\partial r}\frac{\partial^2 r}{\partial x\partial y} + \left(\frac{\partial^2\tilde{\kappa}}{r\partial r\partial\theta}\frac{\partial r}{\partial x} + \frac{\partial^2\tilde{\kappa}}{r^2\partial\theta^2}\frac{r\partial\theta}{\partial x}\right)\frac{r\partial\theta}{\partial y} + \frac{\partial\tilde{\kappa}}{r^2\partial\theta}\frac{r^2\partial^2\theta}{\partial x\partial y} \\
&= \left(-\frac{\partial V_\theta}{\partial r}\sin\theta\cos\theta - \frac{\partial V_r}{\partial r}\sin^2\theta + \frac{V_\theta}{r}\sin\theta\cos\theta\right) + \frac{\partial V_r}{\partial r}\cos^2\theta - \frac{V_r}{r}(1-2\cos^2\theta) - \frac{\partial V_r}{r\partial\theta}\sin\theta\cos\theta\ ,
\end{aligned} \tag{A8}$$

$$\begin{aligned}
\omega_x &= \frac{\partial V_z}{\partial y} - \frac{\partial V_{\tilde{y}}}{\partial z} \\
&= -\left(\frac{\partial V_\theta}{\partial r}\sin\theta - \frac{\partial V_r}{\partial r}\cos\theta\right)\cos\varphi - \left(-\left(\frac{\partial V_\theta}{\partial r}\sin\theta - \frac{\partial V_r}{\partial r}\cos\theta\right)\cos\varphi\right) = 0\ ,
\end{aligned} \tag{A9}$$

ACCEPTED MANUSCRIPT
Physics of Fluids
AIP Publishing
This is the author's peer reviewed, accepted manuscript. However, the online version of record will be different from this version once it has been copyedited and typeset.
PLEASE CITE THIS ARTICLE AS DOI: 10.1063/5.0332888

$$\begin{aligned}\omega_y &= \frac{\partial V_{\tilde{x}}}{\partial z} - \frac{\partial V_z}{\partial x} \\ &= -\left(\frac{\partial V_\theta}{\partial r}\cos\theta + \frac{\partial V_r}{\partial r}\sin\theta\right)\cos\varphi - \left(-\left(\frac{\partial V_\theta}{\partial r}\cos\theta + \frac{\partial V_r}{\partial r}\sin\theta\right)\cos\varphi\right) = 0\end{aligned} \tag{A10}$$

and

$$\begin{aligned}\omega_z &= \frac{\partial V_{\tilde{y}}}{\partial x} - \frac{\partial V_{\tilde{x}}}{\partial y} \\ &= \left(-\frac{\partial V_\theta}{\partial r}\sin\theta\cos\theta - \frac{\partial V_r}{\partial r}\sin^2\theta + \frac{V_\theta}{r}\sin\theta\cos\theta\right) + \frac{\partial V_r}{\partial r}\cos^2\theta - \frac{V_r}{r}(1-2\cos^2\theta) - \frac{\partial V_r}{r\partial\theta}\sin\theta\cos\theta \\ &- \left[\left(-\frac{\partial V_\theta}{\partial r}\sin\theta\cos\theta + \frac{\partial V_r}{\partial r}\cos^2\theta + \frac{V_\theta}{r}\sin\theta\cos\theta\right) - \frac{\partial V_r}{\partial r}\sin^2\theta - \frac{V_r}{r}(1-2\cos^2\theta) - \frac{\partial V_r}{r\partial\theta}\sin\theta\cos\theta\right] \\ &= 0\ .\end{aligned} \tag{A11}$$

However, the flow field remains rotational especially towards the surface and in the wake[52,62]. In the polar coordinate system, $\tilde{\kappa}$ is a stream function, yielding these non-zero components of ω[52].

The pressure is invariant to the rotation of the Cartesian axes[52,62]. The Laplacian of $\tilde{\kappa}$ required to obtain the viscous term of the pressure field (Eq. 10) is computed as[52]

$$\begin{aligned}\frac{\partial V_{\tilde{x}}}{\partial x} &= \frac{\partial^2\tilde{\kappa}}{\partial x^2} = \frac{\partial}{\partial x}\left(\frac{\partial\tilde{\kappa}}{\partial r}\frac{\partial r}{\partial x} + \frac{\partial\tilde{\kappa}}{r\partial\theta}\frac{r\partial\theta}{\partial x}\right) \\ &= \left(\frac{\partial^2\tilde{\kappa}}{\partial r^2}\frac{\partial r}{\partial x} + \frac{\partial^2\tilde{\kappa}}{r\partial r\partial\theta}\frac{r\partial\theta}{\partial x}\right)\frac{\partial r}{\partial x} + \frac{\partial\tilde{\kappa}}{\partial r}\frac{\partial^2 r}{\partial x^2} + \left(\frac{\partial^2\tilde{\kappa}}{\partial r\partial\theta}\frac{\partial r}{\partial x} + \frac{\partial^2\tilde{\kappa}}{r^2\partial\theta^2}\frac{r\partial\theta}{\partial x}\right)\frac{r\partial\theta}{\partial x} + \frac{\partial\tilde{\kappa}}{r^2\partial\theta}\frac{r^2\partial^2\theta}{\partial x^2} \\ &= -\left(\frac{\partial V_\theta}{\partial r}\cos^2\theta + \frac{\partial V_r}{\partial r}\sin\theta\cos\theta + \frac{V_\theta}{r}(1-\cos^2\theta)\right) - \left(\frac{\partial V_r}{\partial r} - \frac{V_r}{r}\right)\sin\theta\cos\theta + \frac{\partial V_r}{r\partial\theta}\sin^2\theta\ ,\end{aligned} \tag{A12}$$

$$\begin{aligned}\frac{\partial V_{\tilde{y}}}{\partial y} &= \frac{\partial^2\tilde{\kappa}}{\partial y^2} = \frac{\partial}{\partial y}\left(\frac{\partial\tilde{\kappa}}{\partial r}\frac{\partial r}{\partial y} + \frac{\partial\tilde{\kappa}}{r\partial\theta}\frac{r\partial\theta}{\partial y}\right) \\ &= \left(\frac{\partial^2\tilde{\kappa}}{\partial r^2}\frac{\partial r}{\partial y} + \frac{\partial^2\tilde{\kappa}}{r\partial r\partial\theta}\frac{r\partial\theta}{\partial y}\right)\frac{\partial r}{\partial y} + \frac{\partial\tilde{\kappa}}{\partial r}\frac{\partial^2 r}{\partial y^2} + \left(\frac{\partial^2\tilde{\kappa}}{\partial r\partial\theta}\frac{\partial r}{\partial y} + \frac{\partial^2\tilde{\kappa}}{r^2\partial\theta^2}\frac{r\partial\theta}{\partial y}\right)\frac{r\partial\theta}{\partial y} + \frac{\partial\tilde{\kappa}}{r^2\partial\theta}\frac{r^2\partial^2\theta}{\partial y^2} \\ &= -\left(\frac{\partial V_\theta}{\partial r}\sin^2\theta - \frac{\partial V_r}{\partial r}\sin\theta\cos\theta + \frac{V_\theta}{r}(1-\sin^2\theta)\right) + \left(\frac{\partial V_r}{\partial r} - \frac{V_r}{r}\right)\sin\theta\cos\theta + \frac{\partial V_r}{r\partial\theta}\cos^2\theta\ ,\end{aligned} \tag{A13}$$

$$\begin{aligned}\frac{\partial V_z}{\partial z} &= \frac{\partial^2\tilde{\kappa}}{\partial z^2} = \frac{\partial}{\partial z}\left(\frac{\partial\tilde{\kappa}}{\partial r}\frac{\partial r}{\partial z}\right) \\ &= \frac{\partial^2\tilde{\kappa}}{\partial r^2}\frac{\partial r}{\partial z}\frac{\partial r}{\partial z} + \frac{\partial\tilde{\kappa}}{\partial r}\frac{\partial^2 r}{\partial z^2} \\ &= -\left(\frac{\partial V_\theta}{\partial r}\cos^2\varphi + \frac{V_\theta}{r}\sin^2\varphi\right)\ ,\end{aligned} \tag{A14}$$

and

ACCEPTED MANUSCRIPT
Physics of Fluids
AIP Publishing
This is the author's peer reviewed, accepted manuscript. However, the online version of record will be different from this version once it has been copyedited and typeset.
PLEASE CITE THIS ARTICLE AS DOI: 10.1063/5.0332888

$$\begin{aligned}\nabla^2\tilde{\kappa} &= \frac{\partial V_{\tilde{x}}}{\partial x}+\frac{\partial V_{\tilde{y}}}{\partial y}+\frac{\partial V_z}{\partial z}=\frac{\partial^2\tilde{\kappa}}{\partial x^2}+\frac{\partial^2\tilde{\kappa}}{\partial y^2}+\frac{\partial^2\tilde{\kappa}}{\partial z^2}\\ &=-\left(\frac{\partial V_\theta}{\partial r}\cos^2\theta+\frac{\partial V_r}{\partial r}\sin\theta\cos\theta+\frac{V_\theta}{r}(1-\cos^2\theta)\right)-\left(\frac{\partial V_r}{\partial r}-\frac{V_r}{r}\right)\sin\theta\cos\theta\\ &+\frac{\partial V_r}{r\partial\theta}\sin^2\theta-\left(\frac{\partial V_\theta}{\partial r}\sin^2\theta-\frac{\partial V_r}{\partial r}\sin\theta\cos\theta+\frac{V_\theta}{r}(1-\sin^2\theta)\right)\\ &+\left(\frac{\partial V_r}{\partial r}-\frac{V_r}{r}\right)\sin\theta\cos\theta+\frac{\partial V_r}{r\partial\theta}\cos^2\theta-\left(\frac{\partial V_\theta}{\partial r}\cos^2\varphi+\frac{V_\theta}{r}\sin^2\varphi\right)\\ &=-\frac{\partial V_\theta}{\partial r}-\frac{V_\theta}{r}+\frac{\partial V_r}{r\partial\theta}-\frac{\partial V_\theta}{\partial r}\cos^2\varphi-\frac{V_\theta}{r}\sin^2\varphi\ .\end{aligned} \tag{A15}$$

Appendix B: Dimensional Consistency of the Pressure Field Equation

For physical credibility and mathematical rigor, the dimensional analysis of Eq. 23 in Section III is presented as follows.

The fundamental dimensions are defined as Mass [M], Length [L], and Time [T]. In terms of these, the primary variables, operators and parameters that feature in Eq. 23 have the following dimensions:

- $\tilde{\kappa}$: $[\mathrm{L}^2\mathrm{T}^{-1}]$
- ρ: $[\mathrm{ML}^{-3}]$
- V: $[\mathrm{LT}^{-1}]$
- t: $[\mathrm{T}]$
- $\tilde{p}$: $[\mathrm{ML}^{-1}\mathrm{T}^{-2}]$
- p_0: $[\mathrm{ML}^{-1}\mathrm{T}^{-2}]$
- μ: $[\mathrm{ML}^{-1}\mathrm{T}^{-1}]$
- λ: $[\mathrm{ML}^{-1}\mathrm{T}^{-1}]$
- $\nabla\equiv\partial/\partial x$: $[\mathrm{L}^{-1}]$

The pressure field equation is given as

$$\tilde{p}=\left[\frac{\partial\kappa}{\partial t}+\rho\left|\frac{\nabla\kappa}{\rho}\right|^2-\frac{4}{3}\mu\nabla\cdot\left(\frac{\nabla\kappa}{\rho}\right)-p_0\right]-\left(\lambda+\frac{2}{3}\mu\right)\nabla\cdot\left(\frac{\nabla\kappa}{\rho}\right)\ .$$

The principle of dimensional homogeneity requires that each additive term in this equation be evaluated to identical fundamental dimensions. Therefore, each term is analyzed below.

1. Left-Hand Side (LHS)
   The dimension of the mechanical pressure is
   $$[\tilde{p}]=[\mathrm{ML}^{-1}\mathrm{T}^{-2}].$$
2. Right-Hand Side (RHS)
   - The time derivative of the scalar κ field yields the following:
   $$\left[\frac{\partial\kappa}{\partial t}\right]=\left[\frac{\partial(\rho\tilde{\kappa})}{\partial t}\right]=\frac{[\mathrm{ML}^{-3}]\cdot[\mathrm{L}^2\mathrm{T}^{-1}]}{[\mathrm{T}]}=[\mathrm{ML}^{-1}\mathrm{T}^{-2}]$$
   - The product of density and the magnitude of the compressible velocity field yields:
   $$\left[\rho\left|\frac{\nabla\kappa}{\rho}\right|^2\right]=[\mathrm{ML}^{-3}]\cdot\left[\frac{[L^{-1}][\mathrm{ML}^{-3}]\cdot[\mathrm{L}^2\mathrm{T}^{-1}]}{[\mathrm{ML}^{-3}]}\right]^2=[\mathrm{ML}^{-1}\mathrm{T}^{-2}]$$
   - The product of dynamic viscosity and the divergence operator applied to the compressible velocity field yields the following results:
   $$\left[\mu\nabla\cdot\left(\frac{\nabla\kappa}{\rho}\right)\right]=[\mathrm{ML}^{-1}\mathrm{T}^{-1}]\cdot[\mathrm{L}^{-1}]\cdot\frac{[\mathrm{L}^{-1}]\cdot[\mathrm{ML}^{-3}]\cdot[\mathrm{L}^2\mathrm{T}^{-1}]}{[\mathrm{ML}^{-3}]}=[\mathrm{ML}^{-1}\mathrm{T}^{-2}]$$

AIP Publishing Physics of Fluids ACCEPTED MANUSCRIPT
This is the author's peer reviewed, accepted manuscript. However, the online version of record will be different from this version once it has been copyedited and typeset.
PLEASE CITE THIS ARTICLE AS DOI: 10.1063/5.0332888

- The dimension of the stagnation pressure is

$$[p_0] = [\mathrm{ML}^{-1}\mathrm{T}^{-2}].$$

- The product of the viscosity coefficients and the divergence operator applied to the compressible velocity field yields the following:

$$\left[\left(\lambda + \frac{2}{3}\mu\right)\nabla\cdot\left(\frac{\nabla\kappa}{\rho}\right)\right] = [\mathrm{ML}^{-1}\mathrm{T}^{-1}]\cdot[\mathrm{L}^{-1}]\cdot\frac{[\mathrm{L}^{-1}]\cdot[\mathrm{ML}^{-3}]\cdot[\mathrm{L}^{2}\mathrm{T}^{-1}]}{[\mathrm{ML}^{-3}]} = [\mathrm{ML}^{-1}\mathrm{T}^{-2}]$$

The reduction in dimensions of all individual terms of both LHS and RHS yields the identical unit profile of $[\mathrm{M\,L}^{-1}\mathrm{T}^{-2}]$, which physically corresponds to pressure ($\mathrm{N/m}^2$). This uniform reduction rigorously demonstrates the dimensional homogeneity and mathematical consistency of the equation.

[1]T. Nagata, A. Noguchi, K. Kusama, T. Nonomura, A. Komuro, A. Ando, and K. Asai, "Experimental investigation on compressible flow over a circular cylinder at Reynolds number of between 1000 and 5000," Journal of Fluid Mechanics **893** (2020), 10.1017/jfm.2020.221, available at https://doi.org/10.1017/jfm.2020.221 - Last accessed: April 05, 2025.

[2]J. Kleimann and C. Röken, "An Exact Analytical Solution for the Weakly Magnetized Flow around an Axially Symmetric Paraboloid, With Application to Magnetosphere Models," Physics of Fluids **36**, 1–17 (2024), available at https://doi.org/10.1063/5.0215849 - Last accessed: July 02, 2026.

[3]S. Jelínek, P. Belov and M. Karlický, "Numerical Simulations of Oscillations in Solar Corona Excited by Vortex Shedding," The Astrophysical Journal **941**, 1–8 (2022), available at https://doi.org/10.3847/1538-4357/aca40d - Last accessed: November 09, 2025.

[4]M. Anyoji, K. Nose, S. Ida, D. Numata, H. Nagai, and K. Asai, "Development of a Low-Density Wind Tunnel for Simulating Martian Atmospheric Flight," Transactions of the Japan Society for Aeronautical and Space Sciences, Aerospace Technology Japan **9**, 21–27 (2011), available at https://www.jstage.jst.go.jp/article/tastj/9/0/9_0_21/_article - Last accessed: April 05, 2025.

[5]T. O. Amoloye, "Modeling the unsteady wake of an impulsively started circular cylinder using refined potential flow theory," Phys. Scr. **99** (2024), 10.1088/1402-4896/ad4ace, available at https://iopscience.iop.org/article/10.1088/1402-4896/ad4ace - Last accessed: February 01, 2025.

[6]V. Matheswaran and L. S. Miller, "A hybrid potential flow model for shedding flow around a circular cylinder," Journal of Engineering Mathematics **147**, 1–20 (2024), available at https://doi.org/10.1007/s10665-024-10386-8 - Last accessed: March 07, 2026.

[7]V. Matheswaran, T. K. DeLillo, and L. S. Miller, "Vortex shedding from bluff bodies: a conformal mapping approach," Journal of Engineering Mathematics **146**, 1–20 (2024), available at https://doi.org/10.1007/s10665-024-10367-x - Last accessed: March 07, 2026.

[8]S. Li, "Sound emission in a quasi-steady transonic turbulent flow past a circular cylinder," Physical Review Fluids **10**, 1–28 (2025), available at https://doi.org/10.1103/PhysRevFluids.10.034603 - Last accessed: February 15, 2026.

[9]M. Awasthi, S. McCreton, D. J. Moreau, and C. J. Doolan, "Coherent oscillations and acoustic waves in a supersonic cylinder wake," Journal of Fluid Mechanics **1012**, 1–31 (2025), available at https://doi.org/10.1017/jfm.2025.10190 - Last accessed: February 27, 2026.

[10]S. Taneda, "Experimental Investigation of the Wakes behind Cylinders and Plates at Low Reynolds Numbers," Journal of the Physical Society of Japan **11**, 302–307 (1956), available at https://doi.org/10.1143/JPSJ.11.302 - Last accessed: April 05, 2025.

[11]S. C. R. Dennis and G. Z. Chang, "Numerical solutions for steady flow past a circular cylinder at Reynolds numbers up to 100," Journal of Fluid Mechanics **42**, 471–489 (1970), available at https://doi.org/10.1017/S0022112070001428 - Last accessed: April 05, 2025.

[12]M. Coutanceau and R. Bouard, "Experimental Determination of the Main Features of the Viscous Flow in the Wake of a Circular Cylinder in Uniform Translation. Part 1. Steady flow," Journal of Fluid Mechanics **79**, 231–256 (1977), available at https://doi.org/10.1017/S0022112077000135 - Last accessed: February 27, 2023.

[13]M. Coutanceau and R. Bouard, "Experimental Determination of the Main Features of the Viscous Flow in the Wake of a Circular Cylinder in Uniform Translation. Part 2. Unsteady flow," Journal of Fluid Mechanics **79**, 257–272 (1977), available at https://doi.org/10.1017/S0022112077000147 - Last accessed: February 27, 2023.

[14]A. Roshko, "On the Development of Turbulent Wakes from Vortex Streets," National Advisory Committee for Aeronautics , 1–78 (1953), available at https://authors.library.caltech.edu/records/jpc6y-qvc49 - Last accessed: April 05, 2025.

[15]A. Roshko, "Experiments on the Flow Past a Circular Cylinder at Very High Reynolds Number," Journal of Fluid Mechanics **10**, 345–356 (1961), available at http://dx.doi.org/10.1017/S0022112061000950 - Last accessed: August 26, 2020.

[16]P. Parnaudeau, C. Johan, D. Heitz, and E. Lamballais, "Experimental and Numerical Studies of the Flow Over a Circular Cylinder at Reynolds Number 3900," Physics of Fluids **20**, 1–14 (2008), available at https://doi.org/10.1063/1.2957018 - Last accessed: August 26, 2020.

[17]S. Behara and S. Mittal, "Wake transition in flow past a circular cylinder," Physics of Fluids **22**, 1–11 (2010), available at https://doi.org/10.1063/1.3500692 - Last accessed: April 05, 2025.

[18]W. F. Lindsey, "Drag of cylinders of simple shapes," NACA Technical Report , 169–176 (1938), available at https://ntrs.nasa.gov/citations/19930091694 - Last accessed: April 05, 2025.

[19]F. E. Gowen and E. W. Perkins, "Drag of circular cylinders for a wide range of Reynolds numbers and Mach numbers," NACA Technical Note , 1–26 (1952), available at https://ntrs.nasa.gov/citations/19930087134 - Last accessed: April 05, 2025.

[20]J. F. McCarrhy JR and T. Kubota, "A study of wakes behind a circular cylinder at M equal 5.7," AIAA Journa **2**, 629–636 (1964), available at https://doi.org/10.2514/3.2399 - Last accessed: April 05, 2025.

[21]V. Murthy and W. Rose, "Form drag, skin friction, and vortex shedding frequencies for subsonic and transonic crossflows on circular cylinder," 10th Fluid and Plasmadynamics Conference (1977), https://doi.org/10.2514/6.1977-687, available at https://doi.org/10.2514/6.1977-687 - Last accessed: April 05, 2025.

[22]O. Rodriguez, "The circular cylinder in subsonic and transonic flow," AIAA Journal **22**, 1713–1718 (1984), available at https://doi.org/10.2514/3.8842 - Last accessed: April 05, 2025.

[23]J. Ackerman, J. Gostelow, A. Rona, and W. Carscallen, "Base Pressure Measurements on a Circular Cylinder in Subsonic Cross Flow." 38th Fluid Dynamics Conference and Exhibit , 1–14 (2008), available at https://arc.aiaa.org/doi/10.2514/6.2008-4305 - Last accessed: April 05, 2025.

[24]T. Nagata, A. Noguchi, T. Nonomura, K. Ohtani, and K. Asai, "Experimental investigation of transonic and supersonic flow over a sphere for Reynolds numbers of 10^3~10^5 by free-flight tests with schlieren visualiza-

AIP Publishing Physics of Fluids ACCEPTED MANUSCRIPT
This is the author's peer reviewed, accepted manuscript. However, the online version of record will be different from this version once it has been copyedited and typeset.
PLEASE CITE THIS ARTICLE AS DOI: 10.1063/5.0332888

tion," Shock waves **30**, 139–151 (2020), available at https://doi.org/10.1007/s00193-019-00924-0 - Last accessed: April 05, 2025.
[25]A. Sansica, J. C. Robinet, F. Alizard, and E. Goncalves, "Three-dimensional instability of a flow past a sphere: Mach evolution of the regular and Hopf bifurcations," Journal of Fluid Mechanics **855**, 1088–1115 (2018), available at https://doi.org/10.1017/jfm.2018.664 - Last accessed: April 05, 2025.
[26]A. Burbeau and P. Sagaut, "Simulation of a viscous compressible flow past a circular cylinder with high-order discontinuous Galerkin methods," Computers and Fluids **31**, 867–889 (2002), available at https://doi.org/10.1016/S0045-7930(01)00055-X - Last accessed: April 05, 2025.
[27]R. F. Bobenrieth Miserda and R. G. Leal, "Numerical simulation of the unsteady aerodynamic forces over a circular cylinder in transonic flow," 44th AIAA Aerospace Sciences Meeting **22**, 16941–16957 (2006), available at https://doi.org/10.2514/6.2006-1408 - Last accessed: April 05, 2025.
[28]D. A. Lysenko, I. S. Ertesvåg, and K. E. Rian, "Large-Eddy Simulation of the Flow Over a Circular Cylinder at Reynolds Number 3900 Using the OpenFOAM Toolbox," Flow, Turbulence and Combustion **89**, 491–518 (2012), available at https://doi.org/10.1007/s10494-012-9405-0 - Last accessed: April 05, 2025.
[29]C. Y. Xu, B. Hou, Z. Wang, Y. T. Zhang, and J. H. Sun, "Effect of Mach number on the compressible flow past a wavy-axis cylinder," Aerospace Science and Technology **104** (2020), https://doi.org/10.1016/j.ast.2020.105943, available at https://doi.org/10.1016/j.ast.2020.105943 - Last accessed: April 05, 2025.
[30]C. Matar, P. Cinnella, X. Gloerfelt, F. Reinker, and S. aus der Wiesche, "Investigation of non-ideal gas flows around a circular cylinder," Energy **268**, 375–395 (2023), available at https://doi.org/10.1016/j.energy.2022.126563 - Last accessed: April 05, 2025.
[31]J. Hoffmann and D. A. Weiss, "Compressible and Viscous Effects in Transonic Planar Flow around a Circular Cylinder—A Numerical Analysis Based on a Commercially Available CFD Tool," Fluids **8**, 1–28 (2023), available at https://doi.org/10.3390/fluids8060182 - Last accessed: April 05, 2025.
[32]D. Canuto and K. Taira, "Two-dimensional compressible viscous flow around a circular cylinder," Journal of Fluid Mechanics **785**, 349–371 (2015), available at https://doi.org/10.1017/jfm.2015.635 - Last accessed: April 05, 2025.
[33]Y. Liu, Z. Ding, Y. Tao, J. Qu, X. Xie, and X. Qiu, "Numerical study on compressible flow around a circular cylinder in proximity to the wall," Physics of Fluids **35**, 1–17 (2023), available at https://doi.org/10.1063/5.0148846 - Last accessed: April 05, 2025.
[34]J. Shang, "Oscillatory compressible flow around a cylinder," 20th Aerospace Sciences Meeting (1982), https://doi.org/10.2514/6.1982-98, available at https://doi.org/10.2514/6.1982-98 - Last accessed: April 05, 2025.
[35]K. Ishii and K. Kuwahara, "Computation of Compressible Flow Around a Circular Cylinder," 17th Fluid Dynamics, Plasma Dynamics, and Lasers Conference , 1–11 (1984), available at https://doi.org/10.2514/6.1984-1631 - Last accessed: April 05, 2025.
[36]M. Pandolfi and F. Larocca, "Transonic flow about a circular cylinder," Computers and Fluids **17**, 205–220 (1989), available at https://doi.org/10.1016/0045-7930(89)90017-0 - Last accessed: April 05, 2025.
[37]N. Botta, "The inviscid transonic flow about a cylinder," Journal of Fluid Mechanics **301**, 225–250 (1995), available at https://doi.org/10.1017/S0022112095003879 - Last accessed: April 05, 2025.
[38]E. Shirani, "Compressible Flow Around a Circular Cylinder," Journal of Applied Sciences **1**, 472–476 (2001), available at https://doi.org/10.3923/jas.2001.472.476 - Last accessed: April 05, 2025.
[39]C. Xu, L. Chen, and X. Lu, "Effect of Mach number on transonic flow past a circular cylinder," Chinese Science Bulletin **54**, 1886–1893 (2009), available at https://doi.org/10.1007/s11434-009-0325-x - Last accessed: April 05, 2025.
[40]Z. Xia, Z. Xiao, Y. Shi, and S. Chen, "Mach Number Effect of Compressible Flow Around a Circular Cylinder," AIAA Journal **54**, 2004–2009 (2016), available at https://doi.org/10.2514/1.J054420 - Last accessed: April 05, 2025.
[41]I. Rodriguez, B. Eiximeno, L. Gasparino, C. Tur-Mongè, J. Muela, and O. Lehmkuhl, "Compressibility effects on the wake dynamics of a circular cylinder," , 1–6 (2023), available at chrome-extension://efaidnbmnnnibpcajpcglclefindmkaj/https://upcommons.upc.edu/bitstream/2117/394832/1/ETMM14_Rodriguez.pdf - Last accessed: April 05, 2025.
[42]L. V. Rolandi, J. Fontane, T. Jardin, J. Gressier, and L. Joly, "Compressibility effects on the secondary instabilities of the circular cylinder wake," Journal of Fluid Mechanics **966**, 1–25 (2023), available at https://doi.org/10.1017/jfm.2023.430 - Last accessed: April 05, 2025.
[43]K. Xue, Q. Li, and L. Zhao, "Compressibility effect on flow characteristics over a circular cylinder at Reynolds number of 3900," Physics of Fluids **36** (2004), https://doi.org/10.1063/5.0217452, available at https://doi.org/10.1063/5.0217452 - Last accessed: April 05, 2025.
[44]S. Li, J. Yang, and P. Teng, "Data-driven prediction of cylinder-induced unsteady wake flow," Applied Ocean Research **150**, 1–19 (2024), available at https://doi.org/10.1016/j.apor.2024.104114 - Last accessed: April 05, 2025.
[45]I. S. Wallerstein and U. Keshet, "Compressible potential flows around round bodies: Janzen–Rayleigh expansion inferences," Journal of Fluid Mechanics **932**, 1–22 (2022), available at https://doi.org/10.1017/jfm.2021.965 - Last accessed: November 09, 2025.
[46]U. Keshet and Y. Naor, "Compressible Flow in Front of an Axisymmetric Blunt Object: Analytic Approximation and Astrophysical Implications," The Astrophysical Journal **830**, 1–9 (2016), available at https://iopscience.iop.org/article/10.3847/0004-637X/830/2/147 - Last accessed: November 09, 2025.
[47]M. Cherry, T. and G. F. J. Temple, "Flow of a compressible fluid about a cylinder," Proceedings of the Royal Society A:Mathematical and Physical Sciences **192**, 45–79 (1947), available at https://royalsocietypublishing.org/doi/pdf/10.1098/rspa.1947.0138 - Last accessed: April 05, 2025.
[48]D. D. Joseph, "Viscous Potential Flow," Journal of Fluid Mechanics **479**, 191–197 (2003), available at https://doi.org/10.1017/S0022112002003634 - Last accessed: May 15, 2026.
[49]D. D. Joseph, "Potential Flow of Viscous Fluids: Historical Notes," International Journal of Multiphase Flow **32**, 285–310 (2006), available at https://doi.org/10.1016/j.ijmultiphaseflow.2005.09.004 - Last accessed: August 26, 2020.
[50]D. Joseph, T. Funada, and J. Wang, "Potential Flows of Viscous and Viscoelastic Liquids," (2007), available at https://doi.org/10.1017/CBO9780511550928.012 - Last accessed: May 17, 2026.
[51]T. O. Amoloye, "Kwasu Function: A Closed-Form Analytical Solution to the Complete Three-Dimensional Unsteady Compressible Navier-Stokes Equation," 2018 AIAA Aerospace Sciences Meeting, AIAA SciTech Forum (2018), available at https://doi.org/10.2514/6.2018-1288 - Last accessed: August 25, 2020.
[52]T. O. Amoloye, *A Refined Potential Theory for the Incompressible Unsteady Subcritical-Reynolds number Flows on Canonical Bluff Bodies*, Ph.D. thesis, Georgia Institute of Technology (2020), available at http://hdl.handle.net/1853/64150 - Last accessed: January 13, 2021.
[53]T. O. Amoloye, "A Closed-Form Analytical Solution to the Complete Three-Dimensional Unsteady Compressible Navier-Stokes Equations," (2021), preprint (Version 1) available at Research Square https://doi.org/10.21203/rs.3.rs-1157529/v1 - Last accessed: January 3, 2022.
[54]T. O. Amoloye, "Analysis of an Unsteady Incompressible Crossflow on a Stationary Circular Cylinder at Reynolds number 3 900 Using Refined Potential Flow Theory," (2022), preprint (Version 1) available at Research Square https://doi.org/10.21203/rs.3.rs-1723482/v1 - Last accessed: February 4, 2023.
[55]J. D. Anderson, *Fundamentals of Aerodynamics*, 5th ed. (McGraw-Hill, New York, 2011).
[56]F. M. White, *Viscous Fluid Flow*, 3rd ed. (McGraw-Hill, New York, 2006).
[57]C. L. Feffermann, *The Millennium Prize Problems: Existence and Smoothness of the Navier-Stokes* (American Mathematical Society, Providence, RI, 2006) available at https://www.ams.org/publications/authors/books/postpub/mprize - Last accessed: August 25, 2020.
[58]R. Farwig, "From Jean Leray to The Millennium Problem: The Navier–Stokes Equations," Journal of Evolution Equations **21**, 3243–3263 (2021), available at https://link.springer.com/article/10.1007/s00028-020-00645-3- Last accessed: March 19, 2022.

AIP Publishing Physics of Fluids ACCEPTED MANUSCRIPT
This is the author's peer reviewed, accepted manuscript. However, the online version of record will be different from this version once it has been copyedited and typeset.
PLEASE CITE THIS ARTICLE AS DOI: 10.1063/5.0332888

[59]J. D. Anderson, *Mordern Compressible Flows with Historical Perspectives*, 3rd ed. (McGraw-Hill, New York, 2003).
[60]G. B. Arfken, H. J. Weber, and F. E. Harris, "Chapter 3 - Vector Analysis," in *Mathematical Methods for Physicists (Seventh Edition)* (Academic Press, 2013) pp. 123–203, available at https://doi.org/10.1016/B978-0-12-384654-9.00003-7 - Last accessed: May 17, 2026.
[61]M. Gad-el Hak, "Questions in Fluid Mechanics: Stokes' Hypothesis for a Newtonian, Isotropic Fluid," Journal of Fluids Engineering **117**, 3–5 (1995), available at https://doi.org/10.1115/1.2816816 - Last accessed: August 26, 2020.
[62]H. Schlichting, *Boundary-Layer Theory*, 7th ed. (McGraw-Hill Book Company, New York, 1979).
[63]T. O. Amoloye, L. T. Oladimeji, M. A. Hayajnh, and O. A. Olayemi, "An exposition on some viscosity dependent issues in refined potential flow theory," Unpublished.
[64]J. D. Anderson, *Hypersonics and High-Temperature Gas Dynamics*, 2nd ed. (American Institute of Aeronautics and Astronautics, Inc., Reston, Virginia, 2006).
[65]J. Sinclair and X. Cui, "A theoretical approximation of the shock standoff distance for supersonic flows around a circular cylinder," Physics of Fluids **29**, 1–13 (2017), available at https://doi.org/10.1063/1.4975983 - Last accessed: February 25, 2026.
[66]B. K. Shivamoggi, "Potential Flow Theory Formulation of Parker's Unsteady Solar Wind Model and Nonlinear Stability of Parker's Steady Solar Wind Solution," The Astrophysical Journal **985**, 1–8 (2025), available at https://doi.org/10.3847/1538-4357/adcd64 - Last accessed: May 24, 2026.
[67]K. Scherer, H. Fichtner, H. J. Fahr, C. Röken, and J. Kleimann, "Generalized Multi-polytropic Rankine Hugoniot Relations and The Entropy Condition," The Astrophysical Journal **833**, 1–10 (2016), available at http://dx.doi.org/10.3847/1538-4357/833/1/38 - Last accessed: July 02, 2026.
[68]G. Livadiotis, "Shock Strength in Space and Astrophysical Plasmas," The Astrophysical Journal **809**, 1–21 (2015), available at http://dx.doi.org/10.1088/0004-637X/809/2/111 - Last accessed: July 03, 2026.
[69]Y. Tao, J. Qu, S. Gao, X. Qiu, X. Zhang, and Y. Liu, "Energy evolution in the Kármán vortex street of compressible flow around a circular cylinder," Physics of Fluids **37**, 1–17 (2025), available at https://doi.org/10.1063/5.0254923 - Last accessed: January 10, 2026.
[70]A. G. Kravchenko and P. Moin, "Numerical Studies of Flow Over a Circular Cylinder at $Re_D = 3900$," Physics of Fluids **12**, 403–417 (2000), available at https://doi.org/10.1063/1.870318 - Last accessed: August 26, 2020.
[71]Matlab, "Matlab," MATLAB R2022b - Home Use, The MathWorks, Inc., Natick, Massachusetts, United States. (2022).
[72]M. Van Dyke, *An Album of Fluid Motion*, 4th ed. (The Parabolic Press, Stanford, California 94305-0030, 1988) available at http://courses.washington.edu/me431/handouts/Album-Fluid-Motion-Van-Dyke.pdf - Last accessed: August 26, 2020.
[73]A. Hadjadj and A. Kudryavtsev, "Computation and Flow Visualization in High-Speed Aerodynamics," Journal of Turbulence **6**, 33–81 (2005), available at https://doi.org/10.1080/14685240500209775 - Last accessed: May 24, 2026.
[74]U. Yildiz, D. Vatansever, and B. Celik, "Shock stand-off distances over sharp wedges for thermally non-equilibrium dissociating nitrogen flows," Theoretical and Computational Fluid Dynamics **37**, 799–821 (2023), available at https://doi.org/10.1007/s00162-023-00669-8 - Last accessed: February 26, 2026.
[75]T. D. Economon, "Simulation and Adjoint-Based Design for Variable Density Incompressible Flows with Heat Transfer," AIAA Journal **58**, 757–769 (2020), available at https://doi.org/10.2514/1.J058222 - Last accessed: May 18, 2026.